

Smart panels with velocity feedback control systems using triangularly shaped strain actuators

Paolo Gardonio and Stephen J. Elliott

Institute of Sound and Vibration Research, University of Southampton, Highfield, Southampton SO17 1BJ, United Kingdom

(Received 28 July 2004; revised 2 December 2004; accepted 25 December 2004)

In this paper we present a theoretical study on the active structural acoustic control of a new smart panel with sixteen triangularly shaped piezoelectric patch actuators, having their base edges evenly distributed along the perimeter of the panel, and velocity sensors positioned at the vertices opposite the base edges. The performance is assessed and contrasted with that of a conventional smart panel using a 4×4 array of square piezoelectric patch actuators evenly distributed over the surface of the panel with velocity sensors at their centers. For both systems the control effectiveness and stability of MIMO decentralized or SISO direct velocity feedback control architectures have been analyzed. The two control systems are arranged to generate active damping which reduces the response and sound radiation of the panel in the lightly damped and well separated low-frequency resonances. In particular the new control system can be seen as a set of sixteen “active wedges” which absorb energy from the incident flexural waves to the borders of the panel so that the panel could be considered anechoic. This study shows that the new arrangement with triangularly shaped actuators can achieve better control than the corresponding system using square actuators. © 2005 Acoustical Society of America. [DOI: 10.1121/1.1863092]

PACS numbers: 43.40.Vn, 43.50.Ki [KAC]

Pages: 2046–2064

I. INTRODUCTION

In general, the low-frequency broadband sound transmission through a lightly damped and lightweight panel, such that its response is characterized by well separated resonances below the critical frequency, is controlled by the response of the panel itself at the resonance frequencies and by the radiation efficiencies of the resonant modes.¹ The sensitivity to the radiation efficiencies arises from both the acoustical excitation and sound radiation mechanisms.¹ In order to control low-frequency sound transmission through a panel it is therefore necessary to either move up its first few resonance frequencies by stiffening the panel or to apply damping treatments to the panel in such a way as to reduce its response at resonance frequencies.¹ Both types of treatments require substantial variations to the structure of the panel which have several drawbacks such as, for example, the change of geometry and weight of the partition and increase of costs. Alternatively, active control techniques could be used, the most attractive of which have the actuators and sensors integrated onto the partition itself in such a way as to create a smart panel for the implementation of active structural acoustic control (ASAC).^{2–5} The control system linking these actuators to these sensors increasingly uses a feedback rather than feed-forward arrangement, because of its ability to deal with broadband random or transient disturbances without an external reference signal.⁶

During the past decade a lot of research work has been carried out to develop ASAC systems to be embedded on thin partitions in order to form compact and possibly lightweight smart panels.^{2–5} Several configurations have been studied that could be grouped into two main families: first, single input single output (SISO) classic feedback control systems^{3,7} using collocated and dual^{8,9} distributed sensor-

actuator pairs which are arranged in such a way as to control radiation modes of panels^{2,10–12} and, second, SISO or multi-input multi-output (MIMO) modern feedback control systems^{3,7} where H_2 or H_∞ optimum state regulators are designed in a LQR/LQG framework, with a state observer based on radiation filters.^{13–15} The advantage of the classic approach is given by the possibility of implementing relatively simple direct feedback control loops that produce active damping⁷ and thus reduces the response of the panel at the low resonance frequencies without sound radiation spillover effects.¹⁶ However, several problems have been encountered in the development of truly collocated and dual^{8,9} distributed sensor-actuator pairs which would guarantee unconditionally stable feedback control loops.^{7,17–24} In contrast the modern approach uses much simpler arrays of sensors and actuators but rather complicated control systems with a state observer that inherently limits the control effectiveness as well as the robustness of the controller.^{3,20,24–37} In summary the development of SISO classic feedback control systems is held back by the difficulties encountered to develop collocated and dual distributed sensor-actuator pairs whose response functions have real part positive definite so that unconditionally stable direct feedback loops could be implemented.^{3,7} In contrast the development of SISO or MIMO modern feedback control systems is held back by the necessity of developing complicated state observers which should be robust to changes of the response of the panel due, for example, to variations of temperature, pressure loading, tensioning effects, etc.

In this context Petitjean and Legrain³⁸ have considered the possibility of simplifying the architecture of a MIMO feedback controller for a smart panel with a 5×3 array of closely located piezoelectric patch sensor-actuator pairs by

implementing decentralized feedback control loops with fixed control gains. In particular they compared the control effectiveness of the decentralized control system with that of a fully coupled MIMO feedback controller and found comparable control results for the two systems. Like a number of authors Elliott *et al.*³⁹ have shown that, provided the sensors and actuators are arranged in collocated and dual pairs, unconditionally stable decentralized feedback loops with fixed gains could be implemented. They have also shown that, if the control systems are arranged to implement active damping, for example with direct velocity feedback loops, then as the control gains are raised up to an optimal value as the response of the panel at resonance frequencies is damped down so that the low-frequency broadband sound transmission is monotonically reduced. References 40 to 42 present the development study of a smart panel with a 4×4 array of decentralized MIMO direct velocity control units which are formed by a square piezoelectric patch actuator with an accelerometer sensor at its center. With this arrangement quite good damping levels have been obtained in the low-frequency resonances of the panel, which have produced reductions of the averaged vibration of the panel between 5 and 8 dB for the third octave bands up to 1 kHz. However, the feedback control gains had to be limited to relatively low values since the decentralized control systems are only conditionally stable as the accelerometer sensor and piezoelectric actuator behaves as a collocated and dual pair only at low frequencies such that the bending wavelength is larger than the dimensions of the piezoelectric patch.⁴²

In this paper, we present a new type of smart panel with sixteen decentralized active damping control units which are composed of triangularly shaped piezoelectric patch actuators, with the base edges aligned along the borders of the panel, and accelerometer sensors placed at the vertices opposite to the base edges of the actuators. The sixteen control units are evenly spaced along the four edges of the panel so that they both look like and work like “active wedges.” The triangular shape of the actuator generates bending moments along the edges plus a transverse point force at the vertex opposite to the base edge⁴³ which results to be collocated and dual with the linear velocity measured by the accelerometer sensor. This makes the sensor actuator pair able to have better collocation and duality features than the one with the square piezoelectric patch actuator. As a result, larger control gains could be implemented in a direct velocity feedback loop which should then produce larger active damping.⁷ Thus, these control units can indeed be considered to be a sort of structural active wedges whose damping effect reduces reflections of incident flexural waves to the edges of the panel which could then be considered to be anechoic. In order to better highlight the control mechanisms and control effects of this type of smart panel with triangularly shaped piezoelectric actuators, the theoretical study presented in this paper contrasts its flexural response and sound radiation with those of a smart panel with a 4×4 array of MIMO-decentralized direct velocity feedback control units evenly distributed over the panel surface which are formed by a square piezoelectric patch actuator with an accelerometer sensor at its center. Also, the effectiveness of simpler control

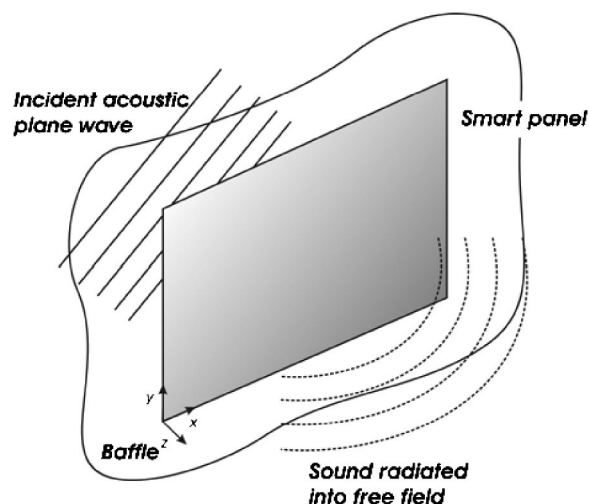


FIG. 1. Physical arrangement considered in a simulation study, in which the vibration of a simply supported panel is excited by a plane acoustic wave on one side and radiates sound into an anechoic half space on the other side of the panel.

configurations is considered for both types of smart panels where the sum of the sixteen velocity outputs is feedback to the sixteen actuators via a fixed gain SISO controller. The sensor-actuator response functions are studied both in frequency domain and with the Nyquist plots in order to assess the stability of the MIMO-decentralized and SISO control configurations.

The paper is structured into four parts. In Sec. II we present the analytical model used to predict the response and sound transmission through the smart panel when it is excited by a plane acoustic wave. In Sec. III the implementation of MIMO-decentralized or SISO direct velocity feedback control loops is modeled and discussed. Finally in Secs. IV and V the main control features of the two smart panels are analyzed and contrasted with reference to MIMO decentralized and SISO feedback control architectures, respectively.

II. RESPONSE AND SOUND TRANSMISSION THROUGH THE SMART PANELS

The steady state flexural response and sound radiation of smart panels which, as shown in Fig. 1, are excited by a harmonic acoustic plane wave, will be used as a model problem to illustrate the effects of the two sensor-actuator arrangements and control architectures shown in Fig. 2. The first arrangement is made by a 4×4 array of square piezoelectric patch actuators with at the centers velocity sensors evenly distributed over the surface of the panel. The second arrangement is instead made by sixteen triangularly shaped piezoelectric patch actuators, with the base edges evenly distributed along the perimeter of the panel, and velocity sensors at the vertices opposite to the base edges. The panel is made of aluminum, with dimensions $l_{xp} \times l_{yp} = 278 \times 247$ mm and thickness $h_p = 1$ mm and it is assumed to be baffled and simply supported along the perimeter. The material and geometrical properties of the panel are summarized in Table I. The far-field sound radiation is determined by the time-averaged total sound power radiated by the panel while

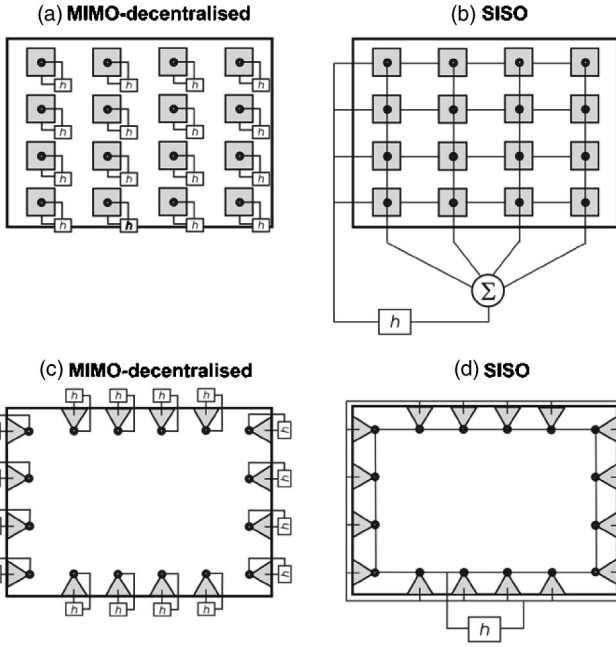


FIG. 2. Smart panels with a 4×4 grid of closely located ideal velocity sensors and square piezoelectric patch actuators or sixteen closely located ideal velocity sensors and triangular piezoelectric patch actuators with the base edges evenly aligned along the four edges of the panel which are arranged either in MIMO-decentralized (type a and c) or SISO (type b and d) direct feedback loops.

its time-averaged total kinetic energy is used to represent the near-field sound radiation which is determined by both strong and weakly radiating modes.¹⁶

The square piezoelectric patches, which have dimensions $a_x \times a_y = 25 \times 25$ mm and thickness $h_{\text{PZT}} = 0.2$ mm, are taken to be evenly distributed over the panel surface so that the distance between the centers of two adjacent patches is given by $d_{sx}, d_{sy} = l_{xp}/4, l_{yp}/4 = 69.5, 61.7$ mm and the distances of the centers of the external patches with the borders of the panel are given by $d_{sx}/2, d_{sy}/2 = 34.8, 30.9$ mm. The square piezoelectric patches, which have base and height dimensions $b, a = 40, 25$ mm and thickness $h_{\text{PZT}} = 0.2$ mm, are instead taken to be evenly distributed along the edges of the panel so that the distances between the centers of the base edges aligned along the $y = 0, l_{yp}$ borders of the panel are given by $d_{tx} = (l_{xp} - 2a)/5 = 45.6$ mm while the distances

TABLE I. Geometry and physical parameters for the panel.

Parameter	Value
Dimensions	$l_{xp} \times l_{yp} = 278 \times 247$ mm
Thickness	$h_p = 1$ mm
Mass density	$\rho_p = 2720$ Kg/m ³
Young's modulus	$E_p = 7 \times 10^{10}$ N/m ²
Poisson ratio	$\nu_p = 0.33$
Modal damping ratio	$\zeta_n = 0.02$

between the centers of the base edges aligned along the $x = 0, l_{xp}$ borders of the panel are given by $d_{ty} = (l_{yp} - 2a)/3 = 65.7$ mm. Also, the centers of the base edges of the outer patches aligned along the $y = 0, l_{yp}$ borders of the panel are located at a distance $d_{ty} + a = 70.6$ mm from the $x = 0, l_{xp}$ border while the centers of the base edges of the outer patches aligned along the $x = 0, l_{xp}$ borders of the panel are located at a distance $a = 25$ mm from the $y = 0, l_{yp}$ border. In this way, as shown in the two bottom schemes of Fig. 2, the vertices of the sixteen triangular patches define a rectangle of dimensions $(l_{xp} - 2a) \times (l_{yp} - 2a)$. The material and geometrical properties of the square and triangular piezoelectric, PZT (lead zirconate titanate), patches are summarized in Table II.

The steady state response of the panel has been derived assuming the incident acoustic plane wave to be harmonic with time dependence of the form $\text{Re}\{\exp(j\omega t)\}$ where ω is the circular frequency and $j = \sqrt{-1}$. The mechanical and electrical functions used in the model have therefore been taken to be the real part of counterclockwise rotating complex vectors, e.g., phasors, given in the form $v(\omega)e^{j\omega t}$ where $v(\omega)$ is the phasor at $t = 0$. A harmonic acoustic wave is assumed to excite the panel with azimuthal and elevation angles of $\phi = 45^\circ$ and $\theta = 45^\circ$ so that it excites all the structural modes of the panel. The sound pressure field $p_i(x, y, t)$ in the plane of the plate is therefore given by

$$p_i(x, y, t) = \text{Re}\{p_i(\omega)e^{j(\omega t - k_x x - k_y y)}\}, \quad (1)$$

where $p_i(\omega)$ is the phasor of the incident wave, $k_x = k_0 \sin(\theta)\cos(\phi)$ and $k_y = k_0 \sin(\theta)\sin(\phi)$ are the acoustic wave numbers in x - and y -directions where $k_0 = \omega/c_0$ and $c_0 = 343$ m/s are, respectively, the acoustic wave number and speed of sound in air.

TABLE II. Geometry and physical parameters for the piezoelectric, PZT (lead zirconate, titanate), patches.

Parameter	Value
Dimensions of the square patches	$a_x \times a_y = 25 \times 25$ mm
Base and height dimensions of the triangular patches	$b, a = 40, 25$ mm
Distances between the centers of two square patches	$d_{sx} = 69.5$ mm, $d_{sy} = 61.7$ mm
Distances between the centers of the base edges aligned either along the $y = 0, l_{yp}$ or $x = 0, l_{xp}$ borders of the panel	$d_{tx} = 45.6$ mm, $d_{ty} = 65.7$ mm
Thickness of the square and triangular patches	$h_{\text{PZT}} = 0.2$ mm
Density	$\rho_{\text{PZT}} = 7600$ kg/m ³
Young's modulus	$E_{\text{PZT}} = 6.3 \times 10^{10}$ N/m ²
Poisson ratio	$\nu_{\text{PZT}} = 0.29$
PZT strain/charge constants	$d_{31}^o = 166 \times 10^{-12}$ m/V $d_{32}^o = 166 \times 10^{-12}$ m/V $d_{36}^o = 0$

Both the time-averaged total kinetic energy and time-averaged total sound power radiated have been derived by dividing the panel into a grid of quadrilateral elements whose dimensions have been taken to be $l_{xe}=l_{xp}/(4N_1)$ and $l_{ye}=l_{yp}/(4N_2)$, where N_1 and N_2 are the higher modal orders used in the calculations. The phasors of the complex transverse velocities, $\dot{w}_{er}(\omega)$, at the centers of these R elements have been grouped into the following column vector:

$$\mathbf{w}_e(\omega) \equiv \begin{Bmatrix} \dot{w}_{e1}(\omega) \\ \dot{w}_{e2}(\omega) \\ \vdots \\ \dot{w}_{eR}(\omega) \end{Bmatrix}. \quad (2)$$

The flexural vibration of the smart panel under study is given by the superposition of the acoustic primary excitation generated by the incident plane wave and the structural secondary excitations generated by the control transducers bonded on the panel. Thus, assuming the system is linear, and assuming the radiated pressure has no effect on the panel vibration, then the vector with the phasors of the velocities at the centers of the elements, $\mathbf{w}_e(\omega)$, can be derived with the following matrix relation:

$$\mathbf{w}_e(\omega) = \mathbf{Y}_{ep}(\omega) p_i(\omega) + \mathbf{Y}_{ec}(\omega) \mathbf{v}_c(\omega), \quad (3)$$

where $\mathbf{v}_c(\omega)$ is a vector with the phasors of the complex input voltage signals, $v_{cs}(\omega)$, to the S control piezoelectric transducers:

$$\mathbf{v}_c(\omega) \equiv \begin{Bmatrix} v_{c1}(\omega) \\ v_{c2}(\omega) \\ \vdots \\ v_{cS}(\omega) \end{Bmatrix}. \quad (4)$$

The elements in the two matrices of Eq. (3) have been derived with a finite modal expansion so that⁴⁴

$$Y_{ep}^{r,1}(\omega) = j\omega \sum_{n=1}^N \frac{\psi_n(x_r, y_r) F_{np}(\omega)}{\rho_p h_p l_{xp} l_{yp} (\omega_n^2 - \omega^2 + j2\zeta_n \omega \omega_n)}, \quad (5)$$

$$Y_{ec}^{r,s}(\omega) = j\omega \sum_{n=1}^N \frac{\psi_n(x_r, y_r) F_{nc,s}(\omega)}{\rho_p h_p l_{xp} l_{yp} (\omega_n^2 - \omega^2 + j2\zeta_n \omega \omega_n)}, \quad (6)$$

where ρ_p and h_p are the density and the thickness of the smart panel ζ_n is the modal damping ratio, which was taken to be 0.01 for all modes in these simulations, ω_n and $\psi_n(x, y)$ are, respectively, the n -th natural frequency and natural mode, which for a simply supported panel are given by

$$\omega_n = \sqrt{\frac{D_p}{\rho_p h_p} \left[\left(\frac{n_1 \pi}{l_{xp}} \right)^2 + \left(\frac{n_2 \pi}{l_{yp}} \right)^2 \right]}, \quad (7)$$

$$\psi_n(x, y) = 2 \sin\left(\frac{n_1 \pi x}{l_{xp}}\right) \sin\left(\frac{n_2 \pi y}{l_{yp}}\right), \quad (8)$$

where $D_p = E_p h_p^3 / 12(1 - \nu_p^2)$ is the bending stiffness of the smart panel, with E_p and ν_p the Young's modulus of elasticity and Poisson's ratio, and n_1, n_2 are the two modal integers for the n -th mode. Finally $F_{np}(\omega)$ and $F_{nc,s}(\omega)$ are the two modal excitation terms which are due, respectively, to the primary acoustic excitation generated by the incident plane

wave and to the secondary flexural excitations generated by either the s -th square or s -th triangular piezoelectric patch control actuators bonded on the panel. The modal primary excitation terms, $F_{np}(\omega)$, are obtained by integrating the pressure field generated over the panel surface, that is⁴⁵

$$F_{np}(\omega) = p_i(\omega) \int_0^{l_{xp}} \int_0^{l_{yp}} \psi_n(x, y) e^{-j(k_x x + k_y y)} dx dy \\ = 4 p_i(\omega) I_{n1} I_{n2} l_{xp} l_{yp}, \quad (9)$$

where, if $n_1 \pi \neq \pm \sin \theta \cos \phi (\omega l_{xp} / c_0)$ and $n_2 \pi \neq \pm \sin \theta \sin \phi (\omega l_{yp} / c_0)$,

$$I_{n1} = \frac{n_1 \pi [1 - (-1)^{n_1} e^{-j \sin \theta \cos \phi (\omega l_{xp} / c_0)}]}{[n_1 \pi]^2 - [\sin \theta \cos \phi (\omega l_{xp} / c_0)]^2} \quad (10a)$$

and

$$I_{n2} = \frac{n_2 \pi [1 - (-1)^{n_2} e^{-j \sin \theta \sin \phi (\omega l_{yp} / c_0)}]}{[n_2 \pi]^2 - [\sin \theta \sin \phi (\omega l_{yp} / c_0)]^2}; \quad (10b)$$

and, if $n_1 \pi = \pm \sin \theta \cos \phi (\omega l_{xp} / c_0)$ and $n_2 \pi = \pm \sin \theta \sin \phi (\omega l_{yp} / c_0)$,

$$I_{n1} = (j/2) \operatorname{sgn}(\sin \theta \cos \phi) \quad (11a)$$

and

$$I_{n2} = (j/2) \operatorname{sgn}(\sin \theta \sin \phi). \quad (11b)$$

The modal secondary excitation terms, $F_{nc,s}(\omega)$, are derived by integrating the bending excitation fields generated by the control actuators over the panel surface. According to Ref. 46 and as shown in Fig. 3(a), if the principal axes x', y', z' of the piezoelectric material are aligned along the x, y, z axes of the panel, the s -th square piezoelectric patch actuator produces moment excitations,

$$m_{xs}(x_{es1,3}, y_{es1,3}, t) = \pm \frac{h_s}{2} e_{32}^0 v_{cs}(t), \quad (12a)$$

$$m_{ys}(x_{es2,4}, y_{es2,4}, t) = \pm \frac{h_s}{2} e_{31}^0 v_{cs}(t), \quad (12b)$$

respectively along the horizontal edges 1, 3, with coordinates $x_{cs} - a_x/2 \leq x_{es1,3} \leq x_{cs} + a_x/2$ and $y_{es1,3} = y_{cs} \mp a_y/2$, and along the vertical edges 2, 4, with coordinates $x_{es2,4} = x_{cs} \pm a_x/2$ and $y_{cs} - a_y/2 \leq y_{es2,4} \leq y_{cs} + a_y/2$. The indices 1 to 4 indicate the four edges in anticlockwise order starting from the bottom horizontal edge and, as given in Table II, a_x, a_y are the dimensions of the patches while x_{cs}, y_{cs} are the center coordinates of the s -th patch. Also, as shown in Fig. 3(a), point forces,

$$f_z(x_{vs2,4}, y_{vs2,4}, t) = -f_z(x_{vs1,3}, y_{vs1,3}, t) = \frac{h_s}{2} e_{36}^0 v_{cs}(t), \quad (12c)$$

are exerted at the four vertices of coordinates $(x_{vs1,3}, y_{vs1,3}) = (x_{cs} \mp a_x/2, y_{cs} \mp a_y/2)$, and $(x_{vs2,4}, y_{vs2,4}) = (x_{cs} \pm a_x/2, y_{cs} \mp a_y/2)$ of each patch. In Eqs. (12a)–(12c), h_s is the total thickness of the panel and piezoelectric patch, that is $h_s = h_p + h_{pZT}$. The piezoelectric stress/charge parameters, e_{31}^0, e_{32}^0 and e_{36}^0 , are derived from the following relation:⁴⁶

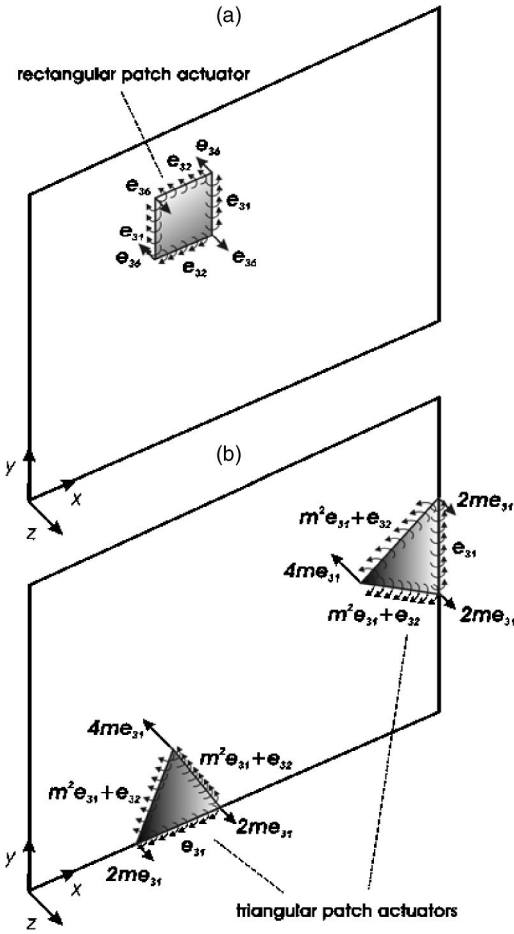


FIG. 3. Panels with square (top) or triangular (bottom) piezoelectric patches.

$$\begin{Bmatrix} e_{31}^0 \\ e_{32}^0 \\ e_{36}^0 \end{Bmatrix} = \begin{bmatrix} \frac{E_{PZT}}{(1-\nu_{PZT}^2)} & \frac{\nu_{PZT}E_{PZT}}{(1-\nu_{PZT}^2)} & 0 \\ \frac{\nu_{PZT}E_{PZT}}{(1-\nu_{PZT}^2)} & \frac{E_{PZT}}{(1-\nu_{PZT}^2)} & 0 \\ 0 & 0 & \frac{E_{PZT}}{2(1+\nu_{PZT})} \end{bmatrix} \times \begin{Bmatrix} d_{31}^0 \\ d_{32}^0 \\ d_{36}^0 \end{Bmatrix}, \quad (13)$$

where the Young's modulus of elasticity, E_{PZT} , the Poisson's ratio, ν_{PZT} , and the piezoelectric strain/charge, d_{31}^0 , d_{32}^0 and d_{36}^0 , parameters of the piezoelectric PZT (lead zirconate, titanate) material considered in this paper are given in Table II. Since the piezoelectric material considered in this paper has $e_{36}^0=0$, then there are no force excitations at the four vertices. Therefore the secondary modal excitation terms for square piezoelectric patch actuators, $F_{nc,s}(\omega)$, are given by the sum of the integrals along the four edges of the piezoelectric patch of the first derivatives of the panel natural modes in directions orthogonal to the edges, pointing outside the square surface, multiplied by the appropriate excitation coefficients given in Eqs. (12a), (12b) that is,

$$\begin{aligned} F_{nc,s}(\omega) = & \frac{h_s}{2} e_{32}^0 \left\{ + \int_{x_{vs1}}^{x_{vs2}} \frac{\partial \psi_n(x, y_{es1})}{\partial y} dx \right. \\ & - \left. \int_{x_{vs3}}^{x_{vs4}} \frac{\partial \psi_n(x, y_{vs3})}{\partial y} dx \right\} \\ & + \frac{h_s}{2} e_{31}^0 \left\{ \int_{y_{vs1}}^{y_{vs4}} \frac{\partial \psi_n(x_{es4}, y)}{\partial x} dy \right. \\ & - \left. \int_{y_{vs2}}^{y_{vs3}} \frac{\partial \psi_n(x_{es2}, y)}{\partial x} dy \right\}. \quad (14) \end{aligned}$$

The bending excitation field generated by a triangular piezoelectric patch has been derived in Ref. 43. Considering the triangular patches shown in Fig. 3(b), which are bonded in such a way as their base edges, a , are aligned with either the x - or y -borders of the panel and assuming that the principal axes x', y', z' of the piezoelectric material are aligned in such a way as x' and y' are parallel, respectively, to the height a and base b of the triangular patches, then the s -th triangular piezoelectric patch actuator produce moment excitations along the base edge of amplitude,

$$m_{bs}(x_{bs}, y_{bs}, t) = \frac{h_s}{2} e_{31}^0 v_{cs}(t), \quad (15a)$$

and moment excitations along the two lateral edges of amplitude,

$$m_{ls1,2}(x_{ls1,2}, y_{ls1,2}, t) = \frac{h_s}{2} (m^2 e_{31}^0 + e_{32}^0) v_{cs}(t). \quad (15b)$$

The positions of the triangular patches have been defined with reference to the middle points of their base edges x_{ms} and y_{ms} . Thus the coordinates of the base edge of the s -th triangular piezoelectric patch actuator are either $x_{ms} - b/2 \leq x_{bs} \leq x_{ms} + b/2$, $y_{bs} = 0, l_{yp}$ or $x_{bs} = 0, l_{xp}$, $y_{ms} - b/2 \leq y_{bs} \leq y_{ms} + b/2$ depending whether the base is aligned along the $y = 0, l_{yp}$ or $x = 0, l_{xp}$ borders of the panel. Also, the coordinates of the lateral edges of the s -th triangular piezoelectric patch actuator with the base aligned along the $y = 0, l_{yp}$ borders of the panel are, respectively, $y_{ls1,2} = \pm m[x_{ls1,2} - (x_{ms} \mp b/2)]$ and $y_{ls1,2} = \mp m[x_{ls1,2} - (x_{ms} \mp b/2)]$ with $x_{ms} - b/2 \leq x_{ls1} \leq x_{ms}$ and $x_{ms} \leq x_{ls2} \leq x_{ms} + b/2$. Finally the coordinates of the lateral edges of the s -th triangular piezoelectric patch actuator with the base aligned along the $x = 0, l_{xp}$ borders of the panel are, respectively, $x_{ls1,2} = \pm m[y_{ls1,2} - (y_{ms} \mp b/2)]$ and $x_{ls1,2} = \mp m[y_{ls1,2} - (y_{ms} \mp b/2)]$ with $y_{ms} - b/2 \leq y_{ls1} \leq y_{ms}$ and $y_{ms} \leq y_{ls2} \leq y_{ms} + b/2$. As listed in Table II, b, a are, respectively, the base and high of the triangular patch and $m = b/2a$ is the slope of the lateral edges. Finally as found for the square piezoelectric patches $h_s = h_p + h_{PZT}$. Also three point forces are generated at the vertices of the s -th triangular piezoelectric patch actuator,

$$f_z(x_{vs1,2}, y_{vs1,2}, t) = 2m \frac{h_s}{2} e_{31}^0 v_{cs}(t), \quad (15c)$$

$$f_z(x_{vs3}, y_{vs3}, t) = -4m \frac{h_s}{2} e_{31}^0 v_{cs}(t), \quad (15d)$$

where the vertices of the s -th triangular piezoelectric patch actuators with the base aligned along the $y=0, l_{yp}$ borders of the panel are, respectively, $x_{vs1,2}=x_{ms} \mp b/2$, $y_{vs1,2}=0, l_y$ and $x_{vs3}=x_{ms}$, $y_{vs3}=a, (l_y-a)$ while the vertices of the s -th triangular piezoelectric patch actuators with the base aligned along the $x=0, l_{xp}$ borders of the panel are, respectively, $x_{vs1,2}=0, l_x$, $y_{vs1,2}=y_{ms} \mp b/2$ and $x_{vs3}=a, (l_x-a)$, $y_{vs3}=y_{ms}$. In summary the secondary modal excitation terms for triangularly shaped piezoelectric patch actuators with the base edge aligned along the perimeter of the panel, $F_{nc,s}(\omega)$, are given by the sum of the integrals along the three edges of the piezoelectric patch of the first derivatives of the natural modes in directions orthogonal to the edges, pointing outside the triangular surface, plus the amplitudes of the modes at the tip vertices multiplied by the appropriate excitation coefficients given, respectively, in Eqs. (15a), (15b), (15d), that is,

$$F_{nc,s}(\omega) = \frac{h_s}{2} (m^2 e_{31}^0 + e_{32}^0) \left\{ \int_{v_{s1}}^{v_{s3}} \frac{\partial \psi_n(x,y)}{\partial \mathbf{n}_{ls1}} dl_{s1} + \int_{v_{s2}}^{v_{s3}} \frac{\partial \psi_n(x,y)}{\partial \mathbf{n}_{ls2}} dl_{s2} \right\} + \frac{h_s}{2} e_{31}^0 \int_{v_{s1}}^{v_{s2}} \frac{\partial \psi_n(x,y)}{\partial \mathbf{n}_{bs}} db_s - 4 \frac{h_s}{2} m e_{31}^0 \psi_n(x_{sv3}, y_{sv3}), \quad (16)$$

where $v_{sj}=(x_{vsj}, y_{vsj})$ indicates the coordinates of the vertices of the triangular patch as given above and $\mathbf{n}_{ls1}, \mathbf{n}_{ls2}, \mathbf{n}_{bs}$ are the normal unit vectors to the lateral and base edges pointing outside the triangular surface of the actuator. Equation (16) does not account for the two forces acting at the base vertices of the triangular patches because the panel is simply supported and therefore does not allow transverse excitations along its perimeter.

The time-averaged total kinetic energy of the panel is given by

$$E(\omega) = \frac{\rho_p h_p}{4} \int_0^{l_{xp}} \int_0^{l_{yp}} |\dot{w}(x,y,\omega)|^2 dx dy, \quad (17)$$

where $\dot{w}(x,y,\omega)$ is the phasor of the transverse velocity over the panel surface. This expression can be approximated by the summation of the kinetic energies of each element into which the panel has been subdivided so that

$$E(\omega) = \frac{M_e}{4} \mathbf{w}_e^H(\omega) \mathbf{w}_e(\omega), \quad (18)$$

where $M_e = \rho_p h_p l_{xe} l_{ye}$ is the mass of each element and H denotes the Hermitian transpose. The time-averaged total sound power radiation by a baffled panel can be derived by integrating the product of the phasor of the nearfield sound pressure, $p_0(x,y,\omega)$, on the radiating surface and the phasor of the transverse velocity of the panel, $\dot{w}(x,y,\omega)$, so that

$$W_r(\omega) = \frac{1}{2} \int_0^{l_{xp}} \int_0^{l_{yp}} \text{Re}[\dot{w}(x,y,\omega)^* p_0(x,y,\omega)] dx dy, \quad (19)$$

where $*$ denotes the complex conjugate. For the baffled flat plate considered in this paper, the acoustic pressure $p_0(x,y,\omega)$ can be written in terms of the surface velocity using the Rayleigh integral¹

$$p_0(x,y,\omega) = \frac{j\omega\rho_0}{2\pi} \int_0^{l_{xp}} \int_0^{l_{yp}} \dot{w}(x',y',\omega) \frac{e^{-jk_0 r}}{r} dx' dy', \quad (20)$$

where $r = \sqrt{(x-x')^2 + (y-y')^2}$ is the distance between the point (x,y) where the sound pressure is estimated and vibration velocity positions on the panel (x',y') and $\rho_0 = 1.21 \text{ kg/m}^3$ is the density of air. Substituting Eq. (20) in (19), the time average total sound radiation is found to be given by a quadruple integral:

$$W_r(\omega) = \frac{\omega\rho_0}{4\pi} \int_0^{l_{xp}} \int_0^{l_{yp}} \int_0^{l_{xp}} \int_0^{l_{yp}} \dot{w}(x,y,\omega)^* \dot{w}(x',y',\omega) \times \frac{\sin k_0 r}{r} dx' dy' dx dy. \quad (21)$$

The quadruple integral in Eq. (21) can also be approximated by summing the radiation contributions of all the elements into which the panel has been subdivided, so that the time-averaged total sound power radiation can be expressed as¹⁶

$$W_r(\omega) = \frac{A_e}{2} \text{Re}[\mathbf{w}_e^H(\omega) \mathbf{p}_e(\omega)], \quad (22)$$

where $A_e = l_{xe} l_{ye}$ is the area of each element and $\mathbf{p}_e(\omega)$ is the vector with the phasors of the sound pressure terms in front of the panel at the center positions of the grid of elements:

$$\mathbf{p}_e(\omega) \equiv \begin{Bmatrix} p_{e1}(\omega) \\ p_{e2}(\omega) \\ \vdots \\ p_{eR}(\omega) \end{Bmatrix}. \quad (23)$$

Following Ref. 16, Eq. (12) can also be written as

$$W_r(\omega) = \frac{A_e}{2} \text{Re}[\mathbf{w}_e^H(\omega) \mathbf{Z}(\omega) \mathbf{w}_e(\omega)] = \mathbf{w}_e^H(\omega) \mathbf{R}(\omega) \mathbf{w}_e(\omega), \quad (24)$$

where $\mathbf{Z}(\omega)$ is the matrix with the point and transfer acoustic impedance terms over the grid of points into which the panel has subdivided:¹² $Z_{ij}(\omega) = (j\omega\rho_0 A_e / 2\pi r_{ij}) e^{-jk_0 r_{ij}}$, with r_{ij} the distance between the centers of the i -th and j -th elements. The matrix \mathbf{R} is defined as the radiation matrix which is given by¹²

$$\mathbf{R}(\omega) = \frac{A_e}{2} \text{Re}[\mathbf{Z}(\omega)] = \frac{\omega^2 \rho_0 A_e^2}{4 \pi c_0} \begin{bmatrix} 1 & \frac{\sin(k_0 r_{12})}{k_0 r_{12}} & \dots & \frac{\sin(k_0 r_{1R})}{k_0 r_{1R}} \\ \frac{\sin(k_0 r_{21})}{k_0 r_{21}} & 1 & & \\ \dots & \dots & \dots & \dots \\ \frac{\sin(k_0 r_{R1})}{k_0 r_{R1}} & & & 1 \end{bmatrix}. \quad (25)$$

Since the primary excitation is an acoustic wave, the ratio of the time-averaged total sound power radiated, $W_r(\omega)$, to the time-averaged incident sound power, $W_i(\omega)$, which is termed the sound transmission ratio;

$$T(\omega) = W_r(\omega)/W_i(\omega), \quad (26)$$

has been used to describe the sound transmission phenomenon. The time-averaged incident sound power due to the plane acoustic wave is given by⁴⁵

$$W_i(\omega) = |p_i(\omega)|^2 l_{xp} l_{yp} \cos(\theta) / 2 \rho_0 c_0. \quad (27)$$

III. DIRECT VELOCITY FEEDBACK CONTROL

The phasors of the output error signal(s), $i_{ce}(\omega)$, from the E velocity error sensors can also be derived with a matrix relation of the type

$$\mathbf{i}_c(\omega) \equiv \mathbf{Y}_{cp}(\omega) p_i(\omega) + \mathbf{Y}_{cc}(\omega) \mathbf{v}_c(\omega), \quad (28)$$

where $\mathbf{i}_c(\omega)$ is the column vector with the phasors of the error sensor signal(s):

$$\mathbf{i}_c(\omega) \equiv \begin{Bmatrix} i_{c1}(\omega) \\ i_{c2}(\omega) \\ \vdots \\ i_{cE}(\omega) \end{Bmatrix}, \quad (29)$$

and $\mathbf{v}_c(\omega)$ is defined in (4). Assuming the velocity sensors used in the smart panels of Fig. 2 to be ideal transducers that measure the transverse velocity at the centers of the square patches or at the tips of the triangular patches, then the elements of the two matrices in Eq. (28) could be derived with a finite modal expansion considering the modal amplitude at the detection points $(x_e, y_e) = (x_{cs}, y_{cs})$ or, $(x_e, y_e) = (x_{vs3}, y_{vs3})$, respectively, for the square and triangular actuators, so that⁴⁴

$$Y_{cp}^r(\omega) = j\omega \sum_{n=1}^N \frac{\psi_n(x_s, y_s) F_{np}(\omega)}{\rho_p h_p l_{xp} l_{yp} (\omega_n^2 - \omega^2 + j2\zeta_n \omega \omega_n)}, \quad (30)$$

$$Y_{cc}^{r,s}(\omega) = j\omega \sum_{n=1}^N \frac{\psi_n(x_s, y_s) F_{nc,s}(\omega)}{\rho_p h_p l_{xp} l_{yp} (\omega_n^2 - \omega^2 + j2\zeta_n \omega \omega_n)}. \quad (31)$$

For the two panels types b and d in Fig. 2, where in order to implement a SISO velocity feedback loop the sensors outputs are summed up and the same control signal is feed to the control actuators, the total current output is still derived with Eq. (28) where the two mobility matrices \mathbf{Y}_{cp} and \mathbf{Y}_{cc} are pre-multiplied by a $1 \times E$ vector \mathbf{e} of unit terms and the matrix \mathbf{Y}_{cc} is also post-multiplied by an $S \times 1$ vector \mathbf{s} of unit

terms so that they become two scalar terms Y_{cp} and Y_{cc} .

The general block diagram of a multi-channel velocity feedback control system is shown in Fig. 4. If an equal number of actuators and velocity sensors is used, the matrix of plant responses, $\mathbf{Y}_{cc}(\omega)$, is square and the matrix of feedback control filters, $\mathbf{H}(j\omega)$, is also square. Provided the control system is stable, the vector with the phasors of the sensor(s) current output(s), $\mathbf{i}_c(\omega)$, is related to the phasor of the incident plane acoustic wave, $p_i(\omega)$, by the expression

$$\mathbf{i}_c(\omega) = [\mathbf{I} + \mathbf{Y}_{cc}(\omega) \mathbf{H}(\omega)]^{-1} \mathbf{Y}_{cp}(\omega) p_i(\omega). \quad (32)$$

Also the vector of control inputs to the actuators, $\mathbf{v}_c(\omega)$, is given by

$$\mathbf{v}_c(\omega) = -\mathbf{H}(\omega) [\mathbf{I} + \mathbf{Y}_{cc}(\omega) \mathbf{H}(\omega)]^{-1} \mathbf{Y}_{cp}(\omega) p_i(j\omega). \quad (33)$$

For single input single output control (SISO) the vectors and matrices reduce to scalars and thus the stability of the feedback control loop could be assessed using the classic feedback control theory.^{3,7,47} In particular, Balas⁹ has shown that, if the sensor-actuator pair is collocated and dual,⁸ then the SISO direct velocity feedback control loop is unconditionally stable. Indeed in this case the sensor-actuator frequency response function is real positive definite⁷ so that its Nyquist plot occupies the right hand side quadrants as ω varies from $-\infty$ to $+\infty$ and thus the Nyquist instability point $(-1 j0)$ is never encircled whatever is the control gain.

For multi-input multi-output (MIMO) decentralized control, $\mathbf{Y}_{cc}(\omega)$ is a fully populated matrix of input and transfer responses between the actuators and sensors on the panel and $\mathbf{H}(\omega)$ is a diagonal matrix which, for direct velocity feedback control, is assumed to have equal fixed gains so that $\mathbf{H}(\omega) = h \mathbf{I}$, where h is the feedback gain. In this case the stability

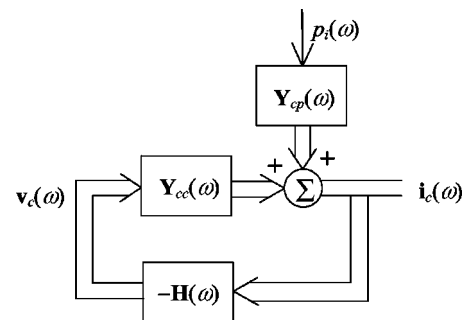


FIG. 4. Multichannel feedback control system, which for a passive plant response, $\mathbf{Y}_{cc}(j\omega)$, and a passive controller $\mathbf{H}(j\omega)$, is unconditionally stable.

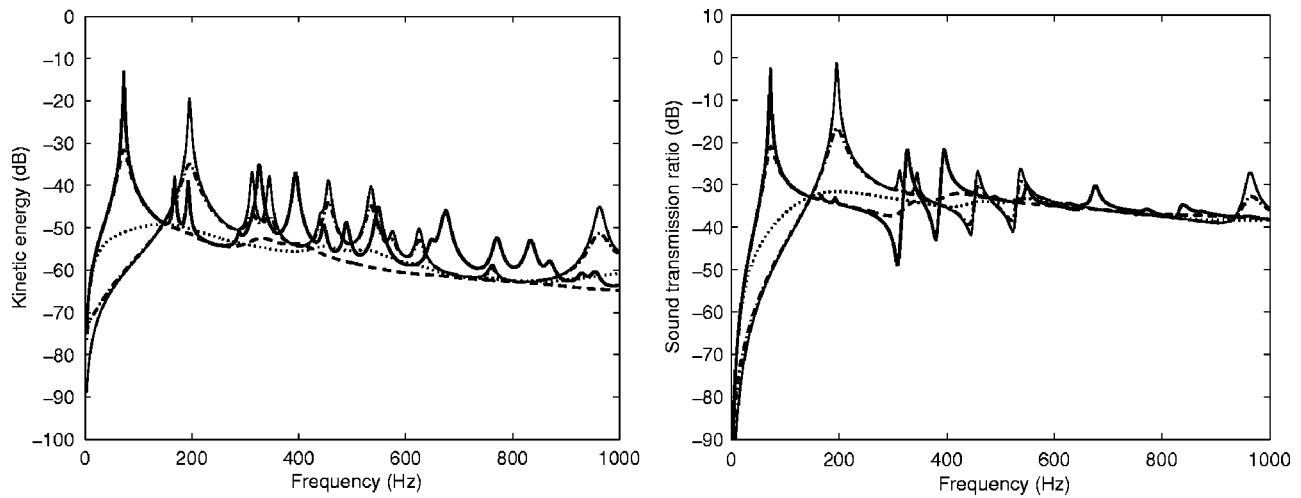


FIG. 5. Total kinetic energy (left) and sound transmission ratio (right) of the panel excited by a plane acoustic wave with no control (solid line) and with a 4×4 grid of closely located velocity sensors and square piezoelectric patches actuators (type a in Fig. 3) MIMO decentralized feedback controllers with feedback gains of 10 (dashed line), 10^2 (dotted line), 10^3 (dash-dotted line) and 10^4 (faint line).

of the MIMO decentralized control system can be determined by examining whether the locus of the determinant of $[\mathbf{I} + \mathbf{Y}_{cc}(j\omega)\mathbf{H}(j\omega)]$ encloses the origin^{48,49} as ω varies from $-\infty$ to $+\infty$. Alternatively the fact that the determinant of a matrix is the product of its eigenvalues can be used to derive a series of polar plots, each of which are analogous to the single channel Nyquist criteria. As found for the SISO control case, if collocated and compatible transducers are used,⁸ then the real part of $\mathbf{Y}_{cc}(\omega)$ must be positive definite and $\mathbf{Y}_{cc}(\omega)$ can be described as being passive. If $\mathbf{H}(\omega)$ is also passive, e.g., when it is equal to $h\mathbf{I}$ and $h > 0$, then the control system is unconditionally stable.^{39,48,49}

When the SISO or MIMO decentralized velocity feedback control systems are implemented, the total kinetic energy and sound transmission ratio given in Eqs. (18) and (24) can be derived after combining Eq. (3) with Eq. (33) so that

$$\mathbf{w}_e(\omega) = \mathbf{Y}_{ep}(\omega)p_i(\omega) - \mathbf{Y}_{ec}(\omega)\mathbf{H}(\omega)[\mathbf{I} + \mathbf{Y}_{cc}(\omega)\mathbf{H}(\omega)]^{-1} \times \mathbf{Y}_{cp}(\omega)p_i(j\omega). \quad (34)$$

It is important to underline that in the following sections the stability properties of the MIMO and SISO control systems in Fig. 2 will be discussed only at a qualitative level. Therefore the control effectiveness of the studied control systems are derived without taking into account whether it would be possible or not to implement the necessary gains without generating instabilities in the control loops.

IV. DECENTRALIZED MIMO DIRECT VELOCITY FEEDBACK CONTROL

In this section the control effectiveness of the smart panels with sixteen decentralized MIMO control units type (a) and type (c) in Fig. 2, which have either sixteen square piezoelectric patch actuators or sixteen triangular piezoelectric patch actuators, is investigated. The stability of the two decentralized control systems is also analyzed to some extent by considering Bode and Nyquist plots of the sensor-actuator frequency response function of one of the sixteen decentralized control systems in the two smart panels. Although the

stability of MIMO control systems should be assessed with reference to the locus of the determinant of $[\mathbf{I} + \mathbf{Y}_{cc}(j\omega)\mathbf{H}(j\omega)]$, for decentralized control, the stability of each control unit could also be evaluated independently using the classic feedback control theory^{3,7,47} which provides an indication of whether the decentralized MIMO control system is to be only conditionally stable. Moreover, if the smart panel is sufficiently damped and the control units are well separated from each others, then an indication about the gain or phase margins for each individual controller could also be derived.

A. Control effectiveness

The two plots in Fig. 5 show, respectively, the total kinetic energy and the sound transmission ratio of the smart panel with the 4×4 array of square piezoelectric patch actuators with the center velocity sensors' MIMO decentralized control system. The solid line on the left hand side plot for the total kinetic energy highlights the typical response of a panel which is characterized by a series of resonances whose amplitudes gradually roll off as the frequency rises. In particular the peaks of the first few resonances are relatively high and sharp because of the low damping effects at lower frequencies. The solid line on the right hand side plot for the sound transmission ratio shows a similar behavior, although there are almost no peaks for the resonances due to the even-even or even-odd natural modes of the panel which have relatively low sound radiation efficiency.¹

The dashed and dotted lines in the two plots of Fig. 5 show that as the gains of the sixteen control systems are raised the resonance peaks are flattened down. This is due to the active damping effect⁵⁰ generated by the sixteen DVFB control systems that indeed increase the overall damping of the lower-frequency resonant modes of the smart panel.^{39,40} However when relatively higher control gains are implemented this trend is inverted and, as shown by the dash-dotted and faint lines in the two plots of Fig. 5, the total kinetic energy and the sound transmission ratio are once more characterized by a new set of low-frequency reso-

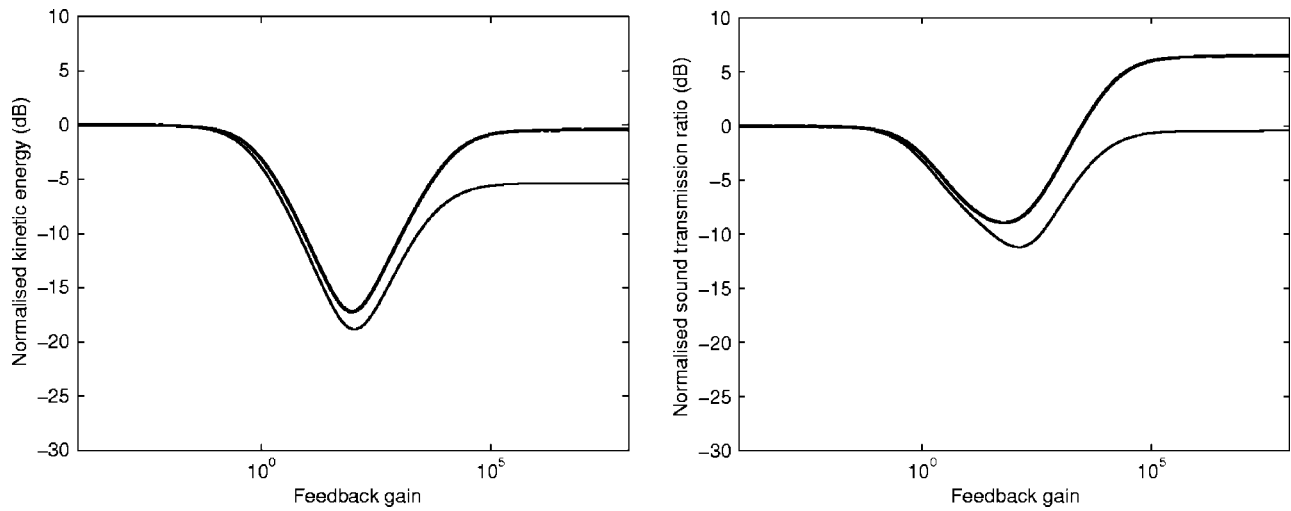


FIG. 6. Normalized total kinetic energy (left) and sound transmission ratio (right), integrated between 0 Hz and 1 kHz, plotted against the gain in the MIMO decentralized velocity feedback controllers, h , for the 4×4 grid of closely located velocity sensors and square piezoelectric patches actuators (solid line, type a in Fig. 2) and the 16 closely located velocity sensors and triangular piezoelectric patches actuators (faint line, type c in Fig. 2).

nances whose amplitudes are similar, if not higher, than those of the panel with no control. This is a typical control spillover phenomenon where, as discussed in Ref. 51, the large control gains produces a pinning effect at the control positions so that the response of the smart panel is rearranged into that of a lightly damped panel which is pinned at the sixteen control positions.

This type of behavior is summarized by the solid lines in the two plots of Fig. 6 which show how the normalized (normalized to the total kinetic energy when there is no control) total kinetic energy and normalized (normalized to the sound transmission ratio when there is no control) sound transmission ratio, integrated from 0 Hz to 1 kHz, vary with the feedback gain. Indeed both plots indicate that as the control gains are raised from zero as the frequency-averaged response and sound radiation of the smart panel monotonically falls down and reductions of the normalized total kinetic energy and normalized sound transmission ratio, respectively, of 17 dB and 9 dB could be achieved. If the control

gains are pushed farther up then, because of the pinning effect described above, the response of the smart panel is brought back to the levels with no control while its sound radiation is even increased by about 6 dB than in the case of no control. This is due to the fact that the new resonant modes of the smart panel generated by the pinning effects at the sixteen control positions have relatively higher sound radiation efficiency than the lower order modes of the unconstrained simply supported panel.¹

The two plots in Fig. 7 show the total kinetic energy and the sound transmission ratio of the smart panel with sixteen triangularly shaped piezoelectric patch actuators with velocity sensors at the vertices opposite to the base edges MIMO decentralized control system. From a qualitative point of view these two plots indicate that the sixteen control units with triangular actuators arranged along the perimeter of the panel produces similar effects than the sixteen control systems with square actuators distributed over the surface of the panel. The most important difference is found when rela-

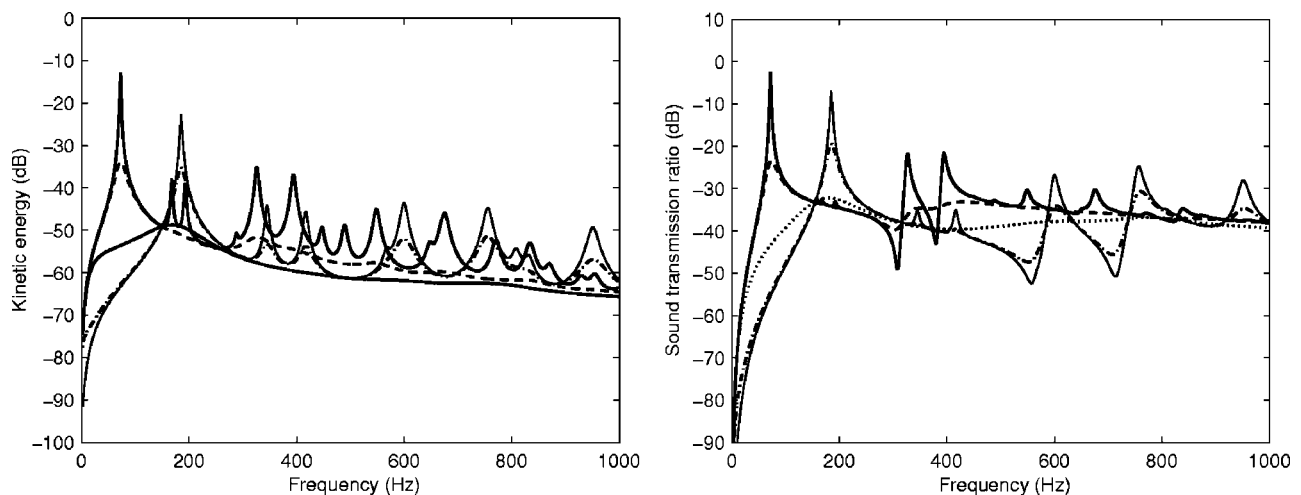


FIG. 7. Total kinetic energy (left) and sound transmission ratio (right) of the panel excited by a plane acoustic wave with no control (solid line) and with 16 closely located velocity sensors and 16 triangular piezoelectric patches actuators (type c in Fig. 2) MIMO decentralized feedback controllers with feedback gains of 10 (dashed line), 10^2 (dotted line), 10^3 (dash-dotted line) and 10^4 (faint line).

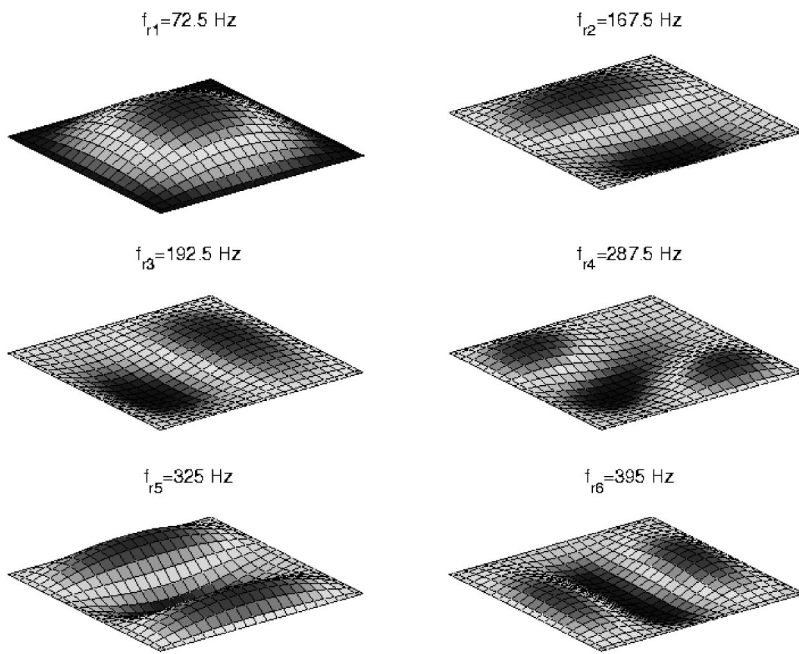


FIG. 8. Deflection shapes of the panel at the first six resonance frequencies with no control.

tively high control gains are implemented in which case the resonances of the new modes of the smart panel, which are generated by the pinning effect of the triangular actuators scattered along the perimeter of the panel, occur at relatively higher frequencies than those due to the pinning effect of the square actuators distributed over the surface of the panel.

Moving to a quantitative analysis the faint lines of the two plots in Fig. 6 indicates that the sixteen control systems with triangular actuators evenly distributed along the perimeter of the smart panel generates slightly larger control effects than those due to the square actuators evenly distributed over the surface of the smart panel. In fact the maximum reduction of the normalized total kinetic energy is increased from 17 dB to 19 dB while the maximum reduction of the normalized sound transmission ratio is increased from 9 dB to 11 dB. As for the smart panel with square actuators evenly distributed over the surface of the smart panel, when relatively large control gains are implemented, the pinning effects at the vertices of the triangular actuators generate a new set of lightly damped resonant modes, which, however, still produce a reduction of about 5 dB of the normalized kinetic energy since in this case the vibrating surface of the panel is reduced to virtual edges defined by the control positions at the tips of the triangular actuators arranged along the edges of the panel. The frequency-averaged sound radiation of the panel is instead brought back to the case with no control, probably because the reduction of the response of the smart panel is balanced by the increased radiation efficiencies of the new resonant modes generated by the pinning effects along the perimeter of the smart panel.

In order to analyze in detail the different behaviors of the two smart panels, the deflections shapes of the panels in correspondence to the first six resonances, which as shown in Fig. 8 are closely linked to the first four natural modes of the panel, have been considered. Figures 9 and 10 show how these six deflection shapes varies when either the optimal control gains, that give the best control effects, or when very

large control gains are implemented in the smart panels with either the sixteen decentralized control systems made by square actuators (left hand side plots) or the sixteen decentralized control systems made by triangular actuators (right hand side plots). Since the deflection shapes occur over a wide range of amplitudes, the plots in Figs. 8 to 10 have been normalized to have the same maximum deflections.

Comparing the two plots in Fig. 9 with that of Fig. 8, it is found that, when the optimal control gains are implemented, then the response of the panel at the first six resonance frequencies is generally modified in such a way that the deflection shapes of the smart panel are not anymore controlled by the co-respective natural modes of the panel. This confirms the active damping action which indeed tends to reduce the contribution of the resonant modes so that the residual response is controlled by nonresonant modes of the panel. It is important to note that the sixteen control units arranged along the perimeter of the smart panel produces the damping action exactly along the borders of the panel which, at frequencies below the critical frequency, are indeed the portions of the panel which generates the sound radiation.¹ Thus the idea of scattering the control units along the perimeter of the smart panel is not convenient just for control stability issues, as discussed in the following section, or for practical matters such as the fact that the central part of the panel is not occupied by the control systems which are instead located near the borders of the panel where it is much easier to arrange the electronics of the sixteen control systems. On the contrary the control units located along the perimeter of the panel generate active damping exactly over the portion of surface of the smart panel that primarily causes sound radiation. Thus the triangularly shaped control actuators arranged along the edges of the panel could indeed be referred as “active structural wedges” that reduce the reflection of incident flexural waves. It is therefore realistic to presume that when localized structural excitations are generated on the panel then even bigger control effects should be

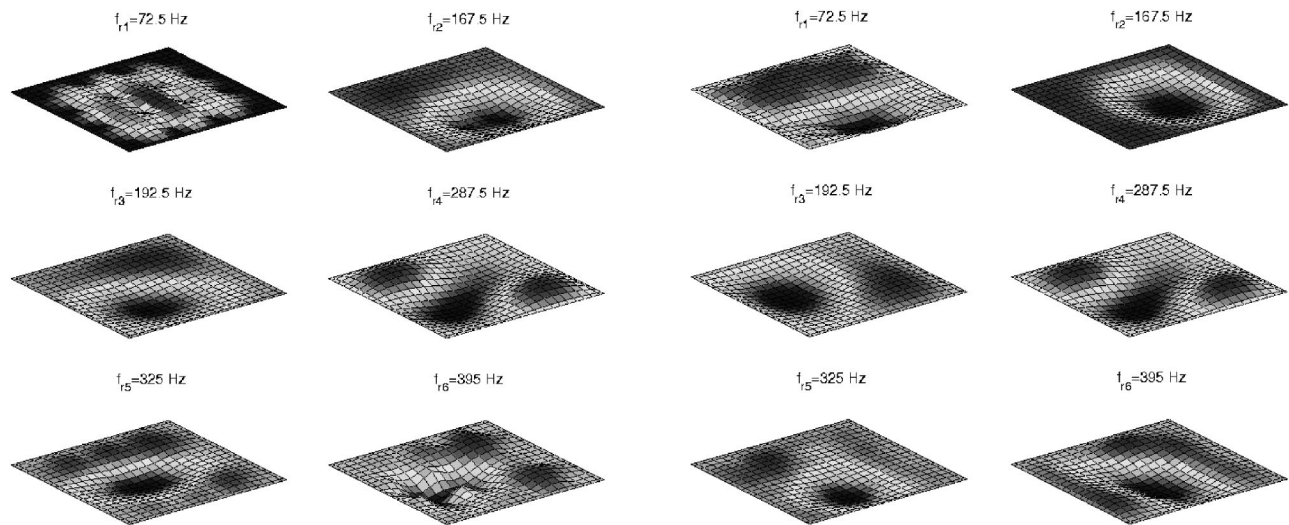


FIG. 9. Deflections shapes of the panel at the first six resonance frequencies when the optimal feedback control gains are implemented in the 4×4 grid of closely located velocity sensors and square piezoelectric patches actuators (left, type a in Fig. 2) and the 16 closely located velocity sensors and triangular piezoelectric patches actuators (right, type c in Fig. 2).

obtained than those found for the incident acoustic wave disturbance.

When very large control gains are implemented in the sixteen control loops then, as shown in the two plots of Fig. 10, the deflection shapes relative to the first six new resonance frequencies clearly show the pinning actions of the control units which, as shown on the left hand side plot, occurs on the 4×4 grid of control points for the system with the square piezoelectric patch actuators or, as shown on the right hand side plot, are located along the perimeter of the panel for the system with the triangular piezoelectric patch actuators. As highlighted by Fahy,¹ a periodically supported panel better radiates sound than a one bay panel since the periodic constraints generates new “edges” around which extra sound is radiated. This is why the frequency-averaged sound radiation of the smart panel constrained by the 4×4 grid of control systems with the square piezoelectric patch

actuators that implement large control gains is about 5 dB higher than that of the unconstrained one-bay panel. In contrast, the sixteen control units with triangular actuators that implement large control gains produce a pinning effect around the edges of the panel such that the deflection shapes are still characterized by a central part which is not constrained. As a result the frequency-averaged sound radiation is about the same to that of the one-bay panel. Essentially, the right hand side plot in Fig. 6, indicates that it is just a little lower probably because the radiating surface of the actively constrained smart panel is smaller than that of the unconstrained panel.

B. Control stability of a single control unit

The stability properties of the two independent control units in Figs. 2(a) and 2(c) are examined using the classic

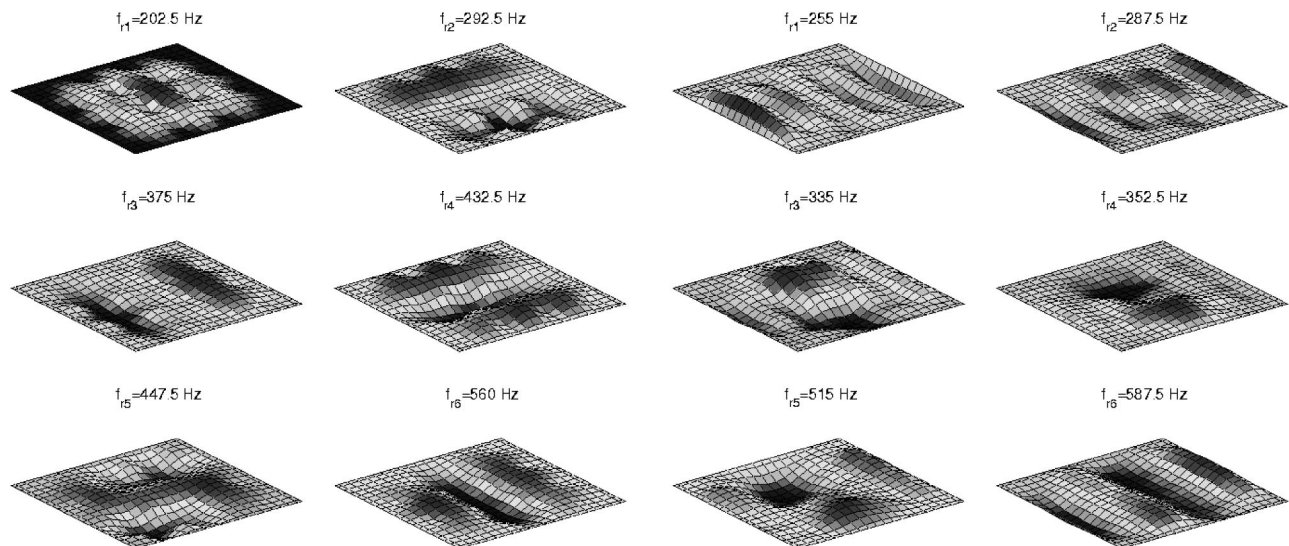


FIG. 10. Deflection shapes of the panel at the first six new resonance frequencies generated by very large feedback gains in the 4×4 grid of closely located velocity sensors and square piezoelectric patches actuators (left, type a in Fig. 2) and the 16 closely located velocity sensors and triangular piezoelectric patches actuators (right, type c in Fig. 2).

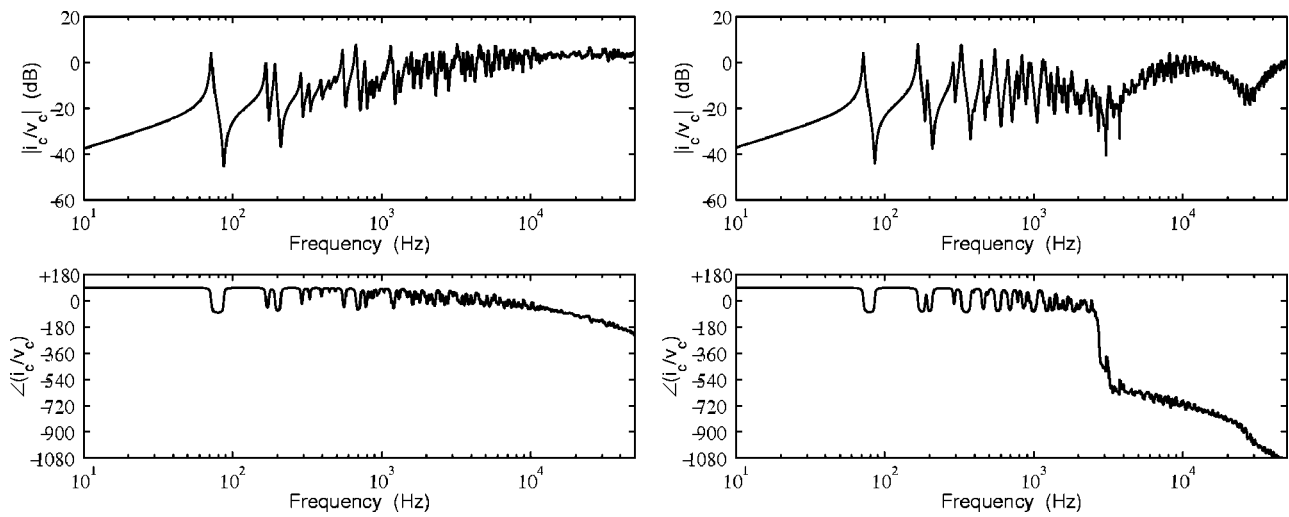


FIG. 11. Frequency response functions of a closely located velocity sensor and square piezoelectric patch actuator control unit (left, type a in Fig. 2) and a closely located velocity sensor and triangular piezoelectric patch actuator (right, type c in Fig. 2).

feedback control theory for SISO feedback control systems.^{3,7,47} The Bode and Nyquist plots of one sensor-actuator feedback loop frequency response function of the two control systems are shown in Figs. 11 and 12.

The left hand side amplitude plot in Fig. 11 highlights the typical feature of square strain actuators which more efficiently excite the panel at higher frequencies so that the amplitude of the sensor-actuator frequency response function grows as the frequency rises.⁵² In contrast the right hand side amplitude plot in Fig. 11 shows that the excitation generated by a triangularly shaped piezoelectric patch is modulated in frequency. This is probably due to a cancellation effect of the moment excitations generated along the lateral edges of the triangular patch in which case the actuation principally occurs via the transverse force generated at the tip of the triangular patch.

The left hand side phase plot of Fig. 11 indicates that the frequency response function generated by the square piezoelectric patch actuator with the velocity sensor at its center is

positive definite up to about 10 kHz. Thus this control system is only conditionally stable.^{3,7,47} Indeed, the Nyquist plot on the left hand side of Fig. 12 suggests that this control system would be unstable even with small feedback control gains since the higher-frequency part of the frequency response functions, with the larger amplitude, would encircle the stability point $-1 + j0$. The right hand side phase plot of Fig. 11 indicates that the frequency response function generated by the triangular piezoelectric patch actuator with the velocity sensor at its tip is positive definite only up to about 2.5 kHz where a sudden phase drop to about -540° occurs. Therefore this control system is also only conditionally stable. However in this case the Nyquist plot on the right hand side of Fig. 12 suggests that for this control system a relatively large gain margin is available since the left hand side of the plot is about five times smaller than the loops on the right hand side. This effect is due to the modulation of the excitation in frequency which combined with the complementary phase drops generates a Nyquist plot with

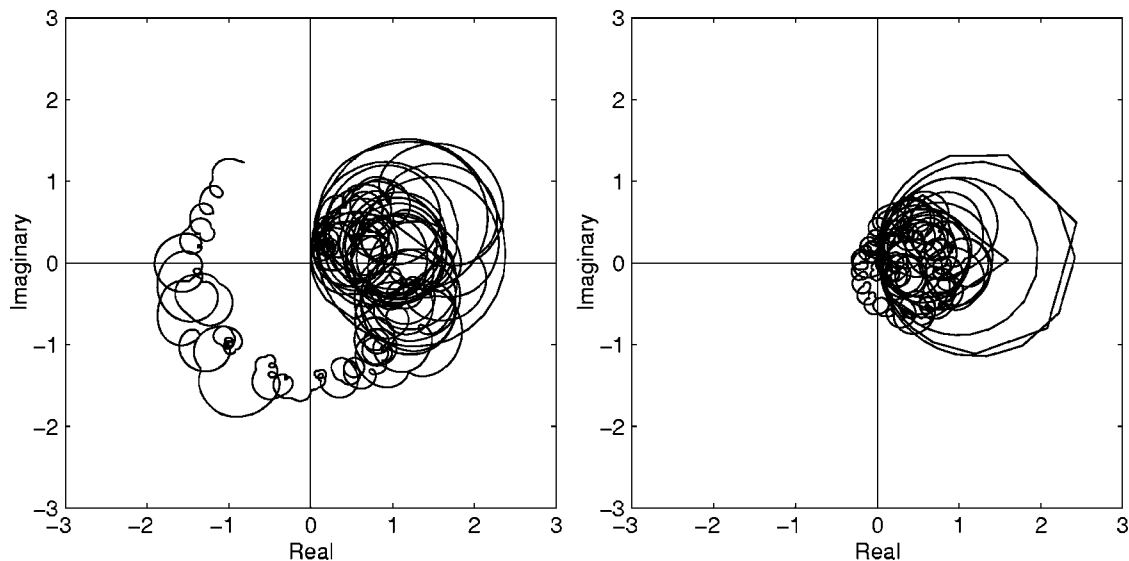


FIG. 12. Nyquist plots for the frequency response functions of a closely located velocity sensor and square piezoelectric patch actuator control unit (left, type a in Fig. 2) and a closely located velocity sensor and triangular piezoelectric patch actuator (right, type c in Fig. 2).

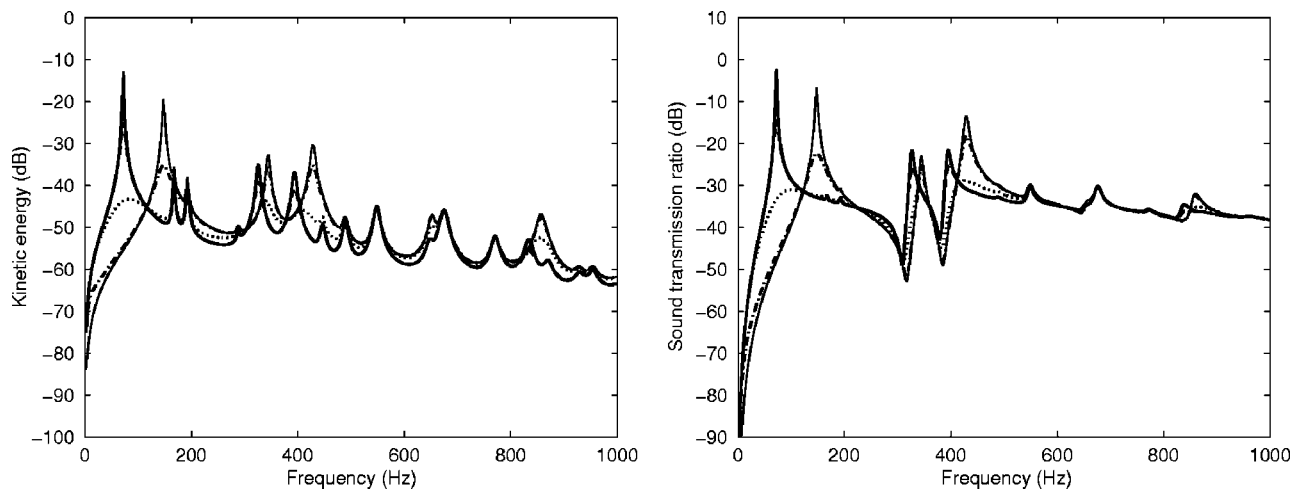


FIG. 13. Total kinetic energy (left) and sound transmission ratio (right) of the panel excited by a plane acoustic wave with no control (solid line) and with a 4×4 grid of closely located velocity sensors and square piezoelectric patches actuators (type b in Fig. 2) SISO feedback controller with feedback gains of 10 (dashed line), 10^2 (dotted line), 10^3 (dash-dotted line) and 10^4 (faint line).

the left hand side squeezed towards the imaginary axis. The modulated excitation of the triangularly shaped actuator depends on the angle of the lateral edges. A trial and error approach has been used in this study to find that the best stability effects are generated by a triangular patch with base $b = 40$ mm and height $a = 25$ mm.

The design of the closely located sensor-actuator control units is an important issue that has been briefly introduced in this section in order to contrast the intrinsic properties of sensor-actuator pairs made with either a square or a triangular strain actuator and an ideal velocity sensor. In practice the local dynamics effects of the sensor should also be taken into consideration as well as the mass and stiffening effects of the piezoelectric patch actuator. A detailed study of these issues is presented in Refs. 41, 53, 54 for a square piezoelectric patch actuator with a velocity sensor at its center.

V. SISO DIRECT VELOCITY FEEDBACK CONTROL

In this section the control effectiveness of the smart panels with SISO control units type (b) and type (d) in Fig. 2, which have either sixteen square piezoelectric patch actuators or sixteen triangular piezoelectric patch actuators driven by a single input signal, is investigated. In this case the stability of the two SISO control systems is fully analyzed by considering Bode and Nyquist plots of the sensor-actuator frequency response function.^{3,7,47}

A. Control effectiveness

The two plots in Fig. 13 show, respectively, the total kinetic energy and the sound transmission ratio of the smart panel with the SISO control system using the 4×4 array of square piezoelectric patch actuators at the center velocity sensors. As found with the MIMO control arrangement, the dashed and dotted lines in the two plots of Fig. 13 show that as the SISO control gain is raised up to an optimal control gain as the active damping generated by the feedback loop levels down most of the resonance peaks. However, in this case the SISO control system does not damp down the resonances due to natural modes of the panel which have no

volumetric vibration component since the sum of the sixteen sensors outputs goes to zero and thus the SISO control loop becomes ineffective. For example, no damping is introduced on the second, third and fourth resonances which are related to the (2,1), (1,2) and (2,2) natural modes of the panel. Beyond the optimal control gain, this trend is inverted and, as shown by the dash-dotted and faint lines, a new set of low-frequency resonances emerge whose amplitudes are similar, if not higher, than those of the panel with no control. Also in this case this phenomenon results from the control spillover effect where a large control gain tends to pin the smart panel at the control positions so that the response of the smart panel is rearranged into that of a lightly damped panel which is pinned at the sixteen control positions.

The two plots in Fig. 14 indicate that, as the control gain is raised as the normalized total kinetic energy and normalized sound transmission ratio, integrated from 0 Hz to 1 kHz, monotonically fall down and reach maximum reductions, respectively, of 12 dB and 8 dB. Therefore the SISO control arrangement is not able to replicate the 17 dB reduction of the total kinetic energy produced by the equivalent MIMO control system. In contrast it nearly generates the 9 dB reduction of the sound transmission ratio produced by the equivalent MIMO control system. This is due to the fact that the error signal used in the SISO feedback control loop is proportional to the volumetric vibration of the smart panel which generates most of the sound radiation at low frequency.^{12,16} When relatively high control gains are implemented then the pinning effect generated at the control positions brings the response of the smart panel back to the levels with no control while its sound radiation is increased by about 2.5 dB than in the case of no control. This is due to the increased sound radiation efficiency of the new resonant modes compared to that of the lower order modes of the unconstrained simply supported panel.¹

The two plots in Fig. 15 show the total kinetic energy and the sound transmission ratio of the smart panel with the SISO control system using the sixteen triangularly shaped piezoelectric patch actuators, with the base edges evenly dis-

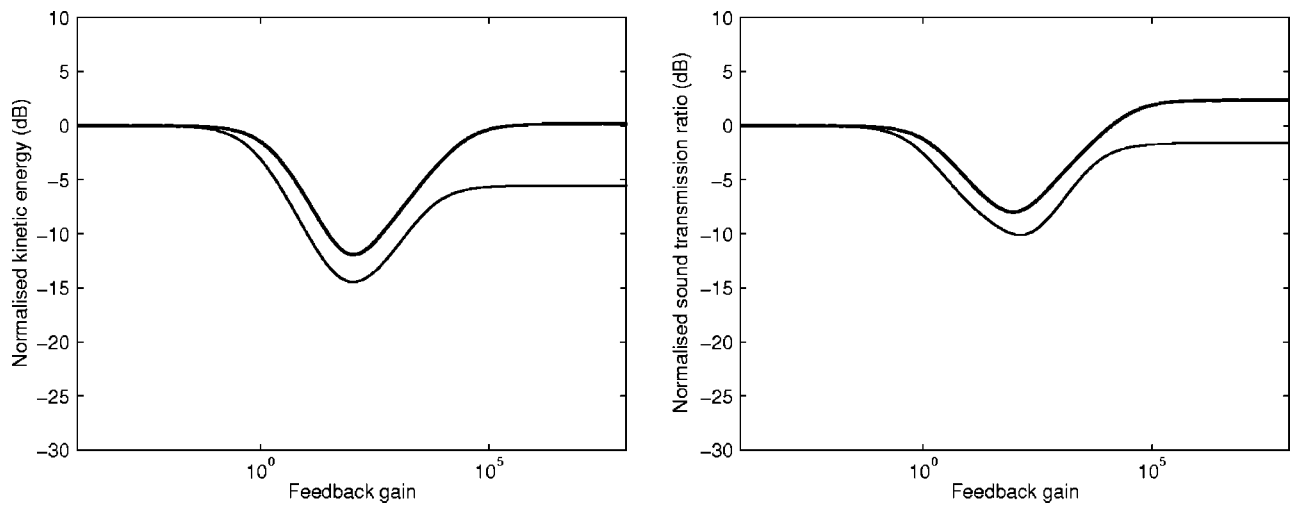


FIG. 14. Normalized total kinetic energy (left) and sound transmission ratio (right), integrated between 0 Hz and 1 kHz, plotted against the gain in the SISO velocity feedback controllers, h , for the 4×4 grid of closely located velocity sensors and square piezoelectric patches actuators (solid line, type b in Fig. 2) and the 16 closely located velocity sensors and triangular piezoelectric patches actuators (faint line, type d in Fig. 2).

tributed along the perimeter of the panel, and velocity sensors at the vertices opposite to the base edges. Comparing the dashed lines in these two plots with those of Fig. 13 it can be noticed that this SISO control system produces at the low-frequency resonances larger damping effects than the SISO control system using the sixteen square actuators. However it still does not generate damping effects at the resonance frequencies related to the natural modes of the panel with no volumetric component. Also, when large control gains, well above the optimal one, are implemented then the SISO control system with the sixteen triangular actuators generates new resonance frequencies some of which occurs at rather different frequencies than those obtained with the SISO control system using square actuators.

This type of behavior is confirmed by the faint lines of the two plots in Fig. 14 which indicates that the SISO arrangement with sixteen triangular actuators brings the maximum reduction of the normalized kinetic energy at 14.5 dB and the maximum reduction of the normalized sound trans-

mission ratio at 10 dB in comparison to the 12 dB and 8 dB, respectively, obtained with the SISO control system using the sixteen square actuators. However, as found for the SISO system with square actuators, the SISO arrangement with sixteen triangular actuators is not able to replicate the 19 dB reduction of the normalized kinetic energy obtained with the equivalent MIMO control system. In contrast it closely generates the 11 dB reduction of the normalized sound transmission ratio produced by the equivalent MIMO control system. Again this is due to the fact that the error signal used in the SISO feedback control loop is proportional to the volumetric vibration of the smart panel which generates most of the sound radiation at low frequency.^{12,16} When relatively high control gains are implemented, then the pinning effect at the sixteen control positions close to the edges of the panel produces a response of the smart panel which is about 5 dB lower than in the case of no control since the vibrating surface has been reduced to that delimited by the sixteen control positions. The frequency-averaged sound radiation of the

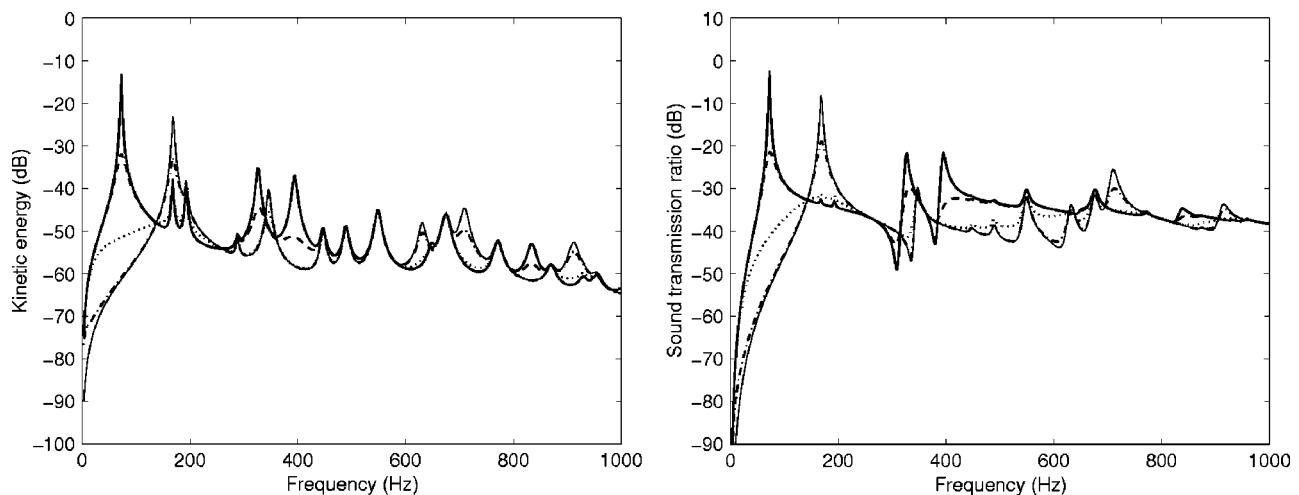


FIG. 15. Total kinetic energy (left) and sound transmission ratio (right) of the panel excited by a plane acoustic wave with no control (solid line) and with 16 closely located velocity sensors and 16 triangular piezoelectric patches actuators (type b in Fig. 2) SISO feedback controller with feedback gains of 10 (dashed line), 10^2 (dotted line), 10^3 (dash-dotted line) and 10^4 (faint line).

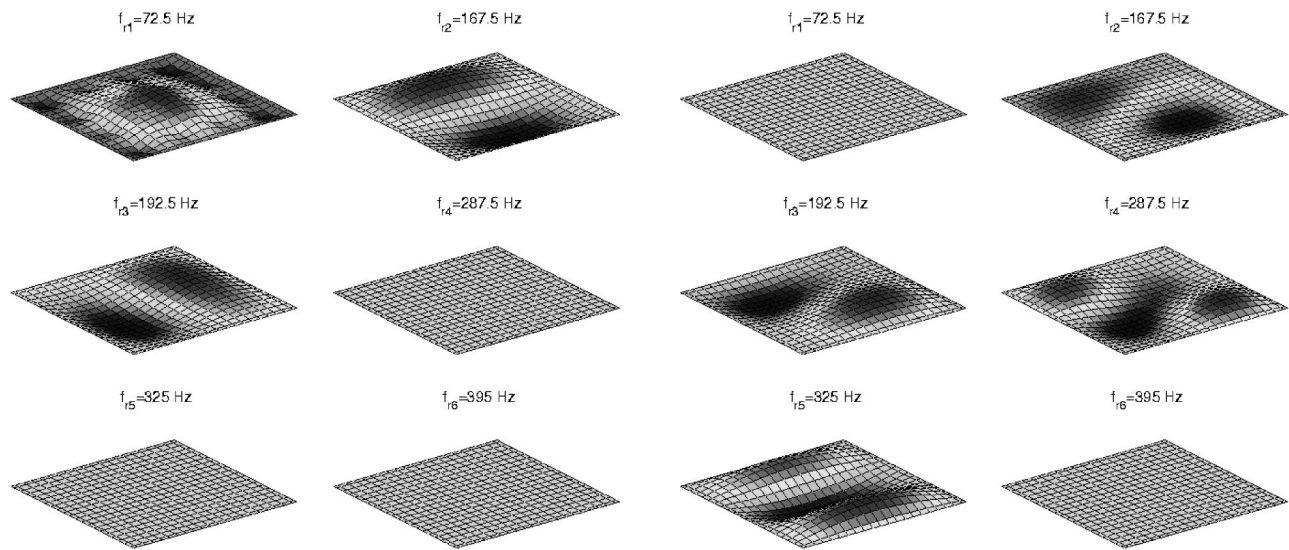


FIG. 16. Deflection shapes of the panel at the first six resonance frequencies when the optimal feedback control gain is implemented in the 4×4 grid of closely located velocity sensors and square piezoelectric patches actuators (left, type b in Fig. 2) and the 16 closely located velocity sensors and triangular piezoelectric patches actuators (right, type d in Fig. 2).

panel is instead reduced by just 2 dB, probably because the reduction of the response of the smart panel is balanced by the increased radiation efficiencies of the new resonant modes generated by the pinning effects along the perimeter of the smart panel.

Figures 16 and 17 show the deflections shapes of the panels in correspondence with the first six resonances when either the optimal control gain, that give the best control effects, or when a very large control gain is implemented in the smart panels with either the SISO control system made with sixteen square actuators (left hand side plots) or the SISO control system made with sixteen triangular actuators (right hand side plots). Also in this case, because the deflection shapes occurs over a wide range of amplitudes, the plots in Figs. 16 and 17 have been normalized to have the same

maximum deflections which are also equal to those in Figs. 8 to 10.

Comparing the two plots in Fig. 16 with that of Fig. 8 indicates that when the optimal control gains of the SISO control systems are implemented, then the response of the panel at some of the first six resonance frequencies is generally modified in such a way as the deflection shapes of the smart panel are not anymore controlled by the co-respective natural modes of the panel. This is due to the active damping action which, as seen for the MIMO control systems, tends to reduce the contribution of the resonant modes. However, as shown by the dashed lines on the left hand side plots in Figs. 13, the SISO control system with square actuators cannot damp down the resonances related to even-even or even-odd modes, such as those at 167.5 and 192.5 Hz relative to

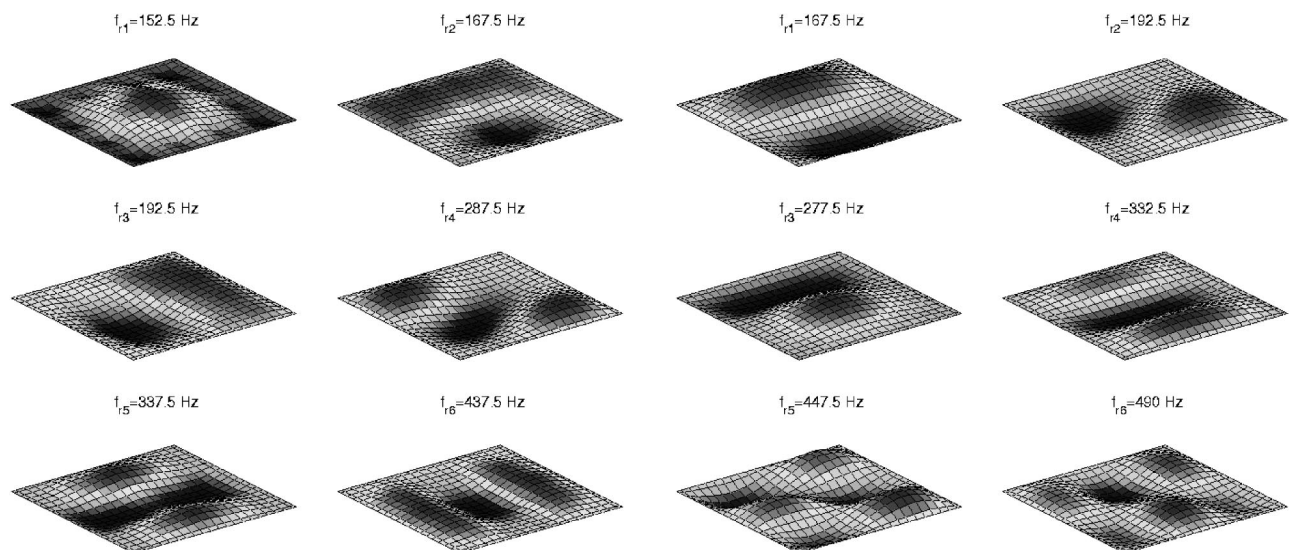


FIG. 17. Deflection shapes of the panel at the first six new resonance frequencies generated by a very large feedback gain in the 4×4 grid of closely located velocity sensors and square piezoelectric patches actuators (left, type b in Fig. 2) and the 16 closely located velocity sensors and triangular piezoelectric patches actuators (right, type d in Fig. 2).

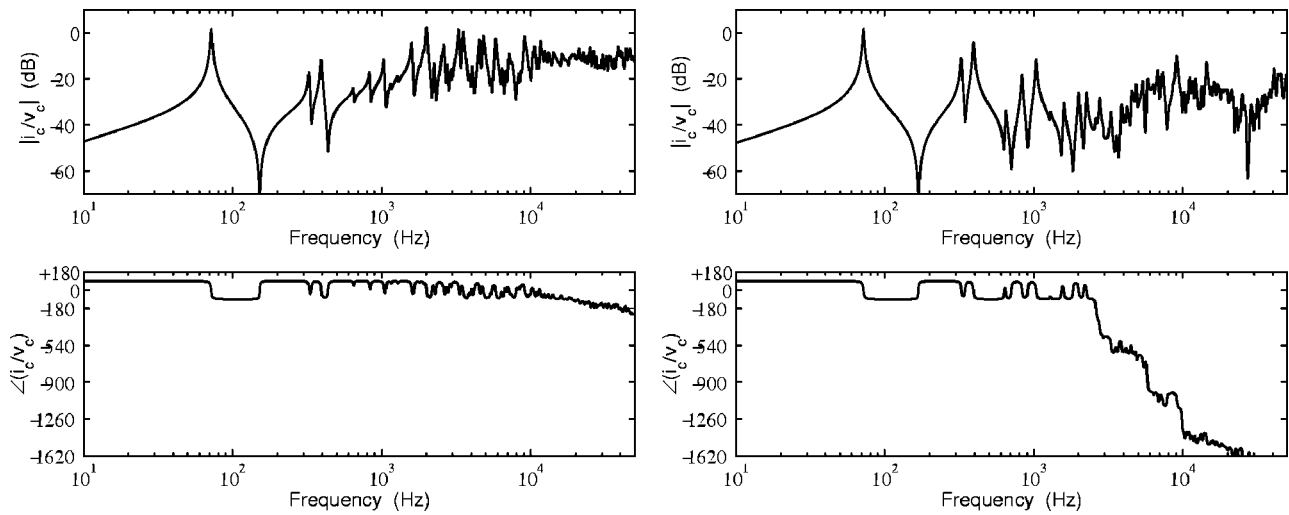


FIG. 18. Frequency response functions of the 4×4 grid of closely located velocity sensors and square piezoelectric patches actuators (left, type b in Fig. 12) and 16 closely located velocity sensors and triangular piezoelectric patches actuators (right, type d in Fig. 2).

the (2,1) and (1,2) modes, and thus the deflection shapes for these two resonance frequencies are exactly the same as those when there is no control. A similar phenomenon is found for the SISO system with triangular actuators arranged along the perimeter of the panel, even though in this case the deflection shapes relative to the resonances at 167.5 and 192.5 Hz are similar to (2,1) and (1,2) natural modes but rotated by an angle of 45° . This is probably due to the combined effects due to the azimuthal angle of the primary acoustic wave and the spacing of the error sensors along the perimeter of the panel. Finally the deflection shapes relative to the second three resonances generated by the system with square actuators and the deflection shapes relative to the first and sixth resonances generated by the system with triangular actuators do not show any type of vibration pattern. This is probably because, as shown by the dotted lines on the left hand side plots of Figs. 13 and 15, the optimal control gains tend to move up these resonance frequencies so that the plots in Fig. 16 show an off-resonance deflection shape.

As shown in the left hand side plot of Fig. 13, when very large control gains are implemented in the SISO control system with square actuators, a new set of resonance frequencies is generated. This is because, as shown on the left hand side plot of Fig. 17, the control actuators produce a 4×4 grid of pinning points that slightly modify the characteristic deflection shapes of the first six resonance frequencies of the unconstrained panel, which are shown in Fig. 8. The left hand side plot in Figs. 15 shows that when very large control gains are implemented in the SISO control system with triangular actuators the new set of resonance frequencies occurs at much higher frequencies. This is because the pinning effect generated by the control actuators generates higher order modes as one can deduce from the deflection shapes of the first six new resonances shown on the right hand side plot of Fig. 17.

B. Control stability

The stability properties of the two SISO control systems which, as shown in Figs. 2(b) and 2(d), are formed either by

a sixteen square piezoelectric patch actuator at the center velocity sensors or by sixteen triangularly shaped piezoelectric patch actuator with velocity sensors at the vertices are investigated using the classic feedback control theory for SISO feedback control systems.^{3,7,47} The Bode and Nyquist plots of the sensor-actuator open loop frequency response functions for the two control systems are therefore shown in Figs. 18 and 19. As found for a single control unit with a square actuator used in the decentralized MIMO control system, the left hand side amplitude plot in Fig. 18 highlights the typical rising trend due to the higher frequency excitation efficiency of square strain actuators⁵² although in this case there is a drop of the amplitude in the frequency range between 100 Hz and 1 kHz and the rising effect is less effective above about 10 kHz. This is probably due to the fact that between 100 Hz and 1 kHz and above 10 kHz the response of the panel is primarily controlled by structural modes with little or no volumetric vibration component so that the sum of the sensor outputs from the sixteen velocity sensors is relatively low. Also, as found for a single control unit with a triangular actuator used in the decentralized MIMO control system, the right hand side amplitude plot in Fig. 18 shows that the excitation generated by the sixteen triangularly shaped piezoelectric patches is modulated in frequency. Moreover in this case there is not an overall rising trend of the excitation so that the amplitude of the sensor-actuator frequency response function in correspondence to resonances below 1 kHz is at least equal to or much higher than those in correspondence to the higher-frequency resonances. This is probably due to a combination of effects where on one hand the excitation generated by the sixteen triangularly shaped actuators is reduced by local cancellation phenomena and on the other hand the sum of the sixteen control signals at the tips of the triangular actuators is also reduced by cancellation phenomena due to the contribution of higher order modes of the panel with a nonvolumetric vibration component.

The left hand side phase plot of Fig. 19 indicates that the frequency response function generated by the square piezoelectric patch actuators with the velocity sensor at their cen-

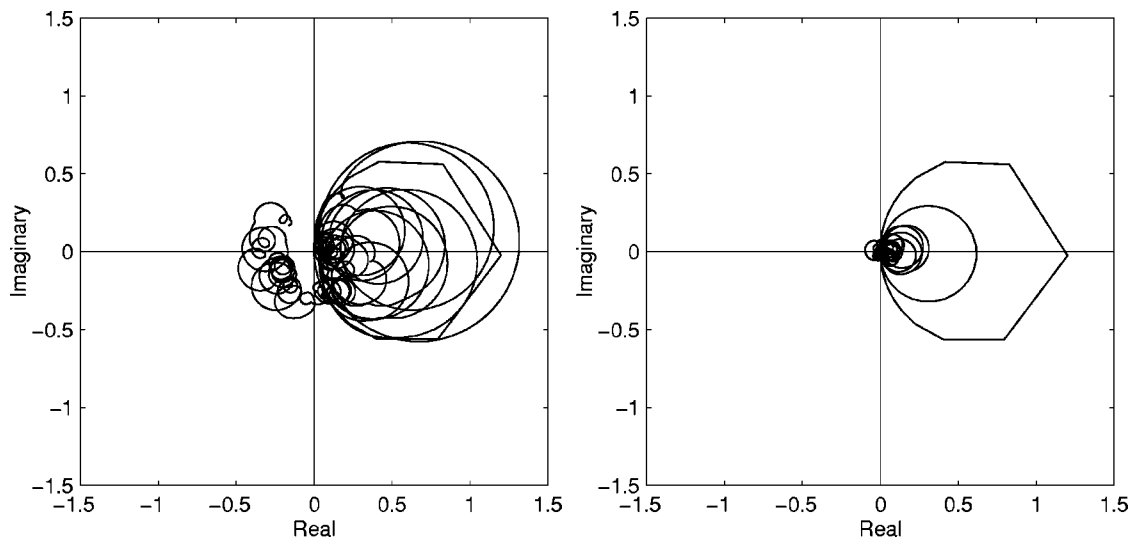


FIG. 19. Nyquist plots for the frequency response functions of the 4×4 grid of closely located velocity sensors and square piezoelectric patches actuators (left, type b in Fig. 2) and 16 closely located velocity sensors and triangular piezoelectric patches actuators (right, type d in Fig. 2).

ters is positive definite up to about 10 kHz so that this SISO control system is only conditionally stable.^{3,7,47} However, since above 10 kHz the amplitude of the frequency response function is about 10 dB lower than those of the first few resonant modes and that in the frequency band between 1 kHz and 10 kHz, the left hand side of the Nyquist plot on the left hand side of Fig. 19 is squeezed towards the imaginary axis so that a limited range of control gains could be implemented without the higher-frequency part of the frequency response function encircling the stability point $-1 + j0$. As found for a single control unit used in the MIMO control system, the right hand side phase plot of Fig. 18 indicates that the frequency response function generated by the sixteen triangular piezoelectric patch actuators with the velocity sensors at their tips is positive definite only up to about 2.5 kHz where a sudden phase drop to -540° occurs which also makes this SISO control system only conditionally stable. However, the fact that the amplitude of the sensor-actuator frequency response function above 1 kHz is modulated in frequency and relatively lower than at frequencies below 1 kHz gives the Nyquist plot shown on the right hand side of Fig. 19 which suggests that for this control system a relatively large gain margin is available. Indeed the left hand side of the Nyquist plot is about twenty times smaller than the loops on the right hand side so that large control gains could be implanted without generating instabilities. The small circles on the left hand side of the Nyquist plot are again due to the combination of periodic drops of the amplitude and co-respective drops of the phase of the sensor-actuator frequency response function.

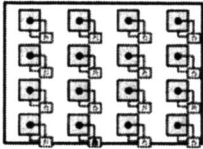
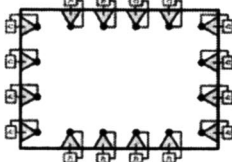
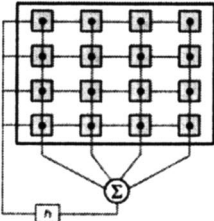
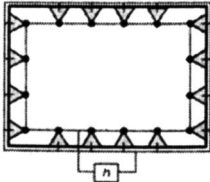
Therefore both SISO control system either with sixteen square control actuators and sixteen velocity sensors at their centers or with sixteen triangular control actuators and sixteen velocity sensors at the vertices could be used to implement direct velocity feedback control. In particular, the system with sixteen triangularly shaped actuators enables the implementation of relatively large control gains without causing instabilities.

VI. CONCLUSIONS

In this study the active structural acoustic control effectiveness of a new smart panel with sixteen triangularly shaped piezoelectric patch actuators having the base edges evenly distributed along the perimeter of the panel and velocity sensors at the vertices opposite to the base edges has been assessed and contrasted with that of a conventional smart panel made by a 4×4 array of square piezoelectric patch actuators evenly distributed over the surface of the panel at the centers velocity sensors. For both systems the control effectiveness and stability issues of MIMO decentralized or SISO velocity feedback control architectures have been analyzed.

As summarized in Table III the MIMO system with square actuators and velocity sensors at their centers relatively large reductions of the integrated kinetic energy and sound transmission ratio between 0 and 1 kHz can be achieved with a maximum value of, respectively, -17 and -9 dB. However the MIMO system with triangular actuators and velocity sensors at the tips produces even larger reductions, respectively, of -19 and -11 dB. Therefore the new system with triangular actuators and velocity sensors at the tips which are evenly distributed along the borders of the panel is not just able to replicate the results of the conventional smart panel with sixteen square piezoelectric patch actuators and velocity sensors at their centers. On the contrary it produces larger control reductions in particular with reference to the far field sound radiation. This is probably due to the fact that the active damping action is generated along the borders of the panel where indeed the sound radiation occurs at low frequencies below coincidence. The same type of behavior is obtained for the case where a SISO control architecture is implemented except that the reductions of the integrated kinetic energy and sound transmission ratio between 0 and 1 kHz go down, respectively, to -12 and -8 dB for the system with square actuators and velocity sensors at their centers and, respectively, to -14.5 and

TABLE III. Maximum frequency-averaged reductions of the total kinetic energy and sound transmission ratio with optimal feedback gains.

Smart panel	Change in kinetic energy dB	Change in sound transmission ratio dB
(a) MIMO-decentralised 	-17	-9
(c) MIMO-decentralised 	-19	-11
(b) SISO 	-12	-8
(d) SISO 	-14.5	-10

- 10 dB for the system with triangular actuators and velocity sensors at the tips. Since for both control arrangements the error sensors are evenly spaced either over the surface of the panel or along its perimeter, then no control signal is generated in correspondence to even-even or even-odd resonant modes which are therefore not controlled. Since the sound radiation efficiency of these modes is relatively low, then this phenomenon has little effect on the overall reduction of the sound radiation but, as confirmed by the data in Table III, it has relatively large effects on the vibration response of the panel and thus on its near field sound radiation.

The stability of one decentralized control unit for the two control arrangements has also been assessed by considering the Bode and Nyquist plots of the sensor-actuator frequency response function. This analysis has indicated that the triangular actuator is less effective at higher frequencies than the square actuator. Also, the triangular shaping generates a point force at the tip of the actuator where the point velocity sensor is placed so that a better collocation effect is obtained than with the square actuator. These two phenom-

ena makes the system with triangularly shaped actuators and velocity sensors at the tips to be relatively more stable so that direct velocity feedback control loops could be implemented up to relatively large control gains. Similar type of results have also been obtained for the SISO control architecture in which case the stability is even enhanced by the fact that the sensor does not measure the vibration contribution of even-even or even-odd resonant modes.

- ¹F. J. Fahy, *Sound and Structural Vibration* (Academic, London, 1985).
- ²C. R. Fuller, S. J. Elliott, and P. A. Nelson, *Active Control of Vibration* (Academic, London, 1996).
- ³R. L. Clark, W. R. Saunders, and G. P. Gibbs, *Adaptive Structures*, 1st ed. (Wiley, New York, 1998).
- ⁴S. J. Elliott and P. Gardonio, "Active vibroacoustic control," in *Responsive Systems For Active Vibration Control*, edited by A. Preumont (Kluwer Academic, London, 2002), pp. 59–82.
- ⁵P. Gardonio, "A review of active techniques for aerospace vibration and noise control," *J. Aircr.* **39**, 206–214 (2002).
- ⁶S. J. Elliott, *Signal Processing for Active Control*, 1st ed. (Academic, London, 2001).
- ⁷A. Preumont, *Vibration Control of Active Structures*, 2nd ed. (Kluwer Academic, London, 2002).
- ⁸J. Q. Sun, "Some observations on physical duality and collocation of structural control sensors and actuators," *J. Sound Vib.* **194**, 765–770 (1996).
- ⁹M. J. Balas, "Direct velocity control of large space structures," *J. Guid. Control* **2**, 252–253 (1979).
- ¹⁰G. V. Borgiotti, "The power radiated by a vibrating body in an acoustic fluid and its determination from boundary measurements," *J. Acoust. Soc. Am.* **88**, 1884–1893 (1990).
- ¹¹K. A. Cunefare, "The minimum multimodal radiation efficiency of baffled finite beams," *J. Acoust. Soc. Am.* **90**, 2521–2529 (1991).
- ¹²S. J. Elliott and M. E. Johnson, "Radiation modes and the active control of sound power," *J. Acoust. Soc. Am.* **94**, 2194–2204 (1993).
- ¹³W. T. Baumann, W. R. Saunders, and H. H. Robertshaw, "Active suppression of acoustic radiation from impulsively excited structures," *J. Acoust. Soc. Am.* **90**, 3202–3208 (1991).
- ¹⁴W. T. Baumann, F.-S. Ho, and H. H. Robertshaw, "Active structural acoustic control of broadband disturbances," *J. Acoust. Soc. Am.* **92**, 1998–2005 (1992).
- ¹⁵R. L. Clark and D. E. Cox, "Multi-variable structural acoustic control with static compensation," *J. Acoust. Soc. Am.* **102**, 2747–2756 (1996).
- ¹⁶M. E. Johnson and S. J. Elliott, "Active control of sound radiation using volume velocity cancellation," *J. Acoust. Soc. Am.* **98**, 2174–2186 (1995).
- ¹⁷S. D. Snyder, N. Tanaka, and Y. Kikushima, "The use of optimally shaped piezoceramic-electric film sensors in the active control of free field structural radiation. Part 2: feedback control," *ASME J. Vibr. Acoust.* **118**, 112–121 (1996).
- ¹⁸P. Gardonio, Y.-S. Lee, S. J. Elliott, and S. Debst, "Analysis and measurement of a matched volume velocity sensor and uniform force actuator for active structural acoustic control," *J. Acoust. Soc. Am.* **110**, 3025–3031 (2001).
- ¹⁹A. Francois, P. De Man, and A. Preumont, "Piezoceramic array sensing of volume displacement: a hardware demonstration," *J. Sound Vib.* **244**, 395–405 (2001).
- ²⁰B. Bingham, M. J. Atalla, and N. W. Hagood, "Comparison of structural-acoustic control designs on an active composite panel," *J. Sound Vib.* **244**, 761–778 (2001).
- ²¹P. De Man, A. Francois, and A. Preumont, "Robust feedback control of a baffled plate via open-loop optimization," *ASME J. Vibr. Acoust.* **124**, 154–157 (2002).
- ²²Y.-S. Lee, P. Gardonio, and S. J. Elliott, "Volume velocity vibration control of a smart panel using a uniform force actuator and an accelerometer array," *J. Smart Mater. Struct.* **11**, 863–873 (2002).
- ²³K. Henriouille and P. Sas, "Experimental validation of collocated PVDF volume velocity sensor/actuator pair," *J. Vibr. Acoust.* **124**, 154–157 (2002).
- ²⁴J. S. Vipperman and R. L. Clark, "Implications of using collocated strain-based transducers for output active structural acoustic control," *J. Acoust. Soc. Am.* **106**, 1392–1399 (1999).

- ²⁵L. Meirovitch and S. Thangjitham, "Control of sound radiation from submerged plates," *ASME J. Vibr. Acoust.* **88**, 402–407 (1990).
- ²⁶R. L. Clark and D. E. Cox, "Multi-variable structural acoustic control with static compensation," *J. Acoust. Soc. Am.* **102**, 2747–2756 (1997).
- ²⁷W. Dehandschutter, K. Henriouille, J. Swevers, and P. Sas, "Feedback control of broadband sound radiation using a volume velocity sensor," *Proceedings of ACTIVE 97*, Budapest, Hungary, 1997, pp. 979–992.
- ²⁸J. S. Vipperman and R. L. Clark, "Acoustic power suppression of a panel structure using H_∞ output feedback control," *J. Acoust. Soc. Am.* **105**, 219–225 (1999).
- ²⁹D. E. Cox, G. P. Gibbs, R. L. Clark, and J. S. Vipperman, "Experimental robust control of structural acoustic radiation," *ASME J. Vibr. Acoust.* **121**, 433–439 (1999).
- ³⁰R. L. Clark and D. E. Cox, "Experimental demonstration of a band-limited actuator/sensor selection strategy for structural acoustic control," *J. Acoust. Soc. Am.* **106**, 3407–3414 (1999).
- ³¹G. C. Smith and R. L. Clark, "Tradeoffs in design complexity—temporal versus spatial compensation," *J. Sound Vib.* **228**, 1182–1194 (1999).
- ³²J. S. Vipperman and R. L. Clark, "Multivariable feedback active structural acoustic control using adaptive piezoelectric sensor/actuators," *J. Acoust. Soc. Am.* **105**, 219–225 (1999).
- ³³G. P. Gibbs, R. L. Clark, D. E. Cox, and J. S. Vipperman, "Radiation modal expansion: application to active structural acoustic control," *J. Acoust. Soc. Am.* **107**, 332–339 (2000).
- ³⁴R. L. Clark and D. E. Cox, "Active control design for acoustic radiation using mixed-norm optimization," *J. Acoust. Soc. Am.* **108**, 1345–1348 (2000).
- ³⁵G. C. Smith and R. L. Clark, "A crude method of loop-shaping adaptive structures through optimum spatial compensator design," *J. Sound Vib.* **247**, 489–508 (2001).
- ³⁶K. Seto, M. Ren, and F. Doi, "Modeling and feedback structural acoustic control of a flexible plate," *ASME J. Vibr. Acoust.* **123**, 18–23 (2001).
- ³⁷W. Chang, S. V. Varadan, and V. K. Varadan, "Design of robust vibration controller for smart panel using finite element model," *ASME J. Vibr. Acoust.* **124**, 265–276 (2002).
- ³⁸B. Petitjean and I. Legrain, "Feedback controllers for active vibration suppression," *Jo. Struct. Control* **3**, 111–127 (1996).
- ³⁹S. J. Elliott, P. Gardonio, T. C. Sors, and M. J. Brennan, "Active vibro-acoustic control with multiple feedback loops," *J. Acoust. Soc. Am.* **111**, 908–915 (2001).
- ⁴⁰P. Gardonio, E. Bianchi, and S. J. Elliott, "Smart panel with multiple decentralised units for the control of sound transmission. Part I: theoretical predictions," *J. Sound Vib.* **274**, 163–192 (2004).
- ⁴¹P. Gardonio, E. Bianchi, and S. J. Elliott, "Smart panel with multiple decentralised units for the control of sound transmission. Part II: design of the decentralized control units," *J. Sound Vib.* **274**, 193–213 (2004).
- ⁴²P. Gardonio, E. Bianchi, and S. J. Elliott, "Smart panel with multiple decentralised units for the control of sound transmission. Part III: control system implementation," *J. Sound Vib.* **274**, 215–232 (2004).
- ⁴³J. M. Sullivan, J. E. Jr. Hubbard, and S. E. Burke, "Modeling approach for two-dimensional distributed transducers of arbitrary spatial distribution," *J. Acoust. Soc. Am.* **99**, 2965–2974 (1996).
- ⁴⁴P. Gardonio and S. J. Elliott, "Driving point and transfer mobility matrices for thin plates excited in flexure," ISVR Technical Report No 277, 1999.
- ⁴⁵B. T. Wang, C. R. Fuller, and E. K. Dimtriadis, "Active control of noise transmission through rectangular plates using multiple piezoelectric or point force actuators," *J. Acoust. Soc. Am.* **90**, 2820–2830 (1991).
- ⁴⁶C. K. Lee, "Theory of laminated piezoelectric plates for the design of distributed sensor/actuators. Part I: governing equations and reciprocal relationships," *J. Acoust. Soc. Am.* **87**, 1144–1158 (1990).
- ⁴⁷L. Meirovitch, *Dynamics and Control of Structures* (Wiley, New York, 1990).
- ⁴⁸S. M. Joshi, *Control of Large Flexible Space Structures* (Springer-Verlag, Berlin, 1989).
- ⁴⁹K. J. Aström and B. Wittenmark, *Adaptive Control*, 2nd ed. (Addison-Wesley, New York, 1995).
- ⁵⁰S. J. Elliott, M. Serrand, and P. Gardonio, "Feedback stability limits for active isolation systems with reactive and inertial actuators," *Trans. ASME, J. Vib. Acoust.* **123**, 250–261 (2001).
- ⁵¹P. Gardonio and S. J. Elliott, "Modal response of a beam with a sensor-actuator pair for the implementation of velocity feedback control," *J. Sound Vib.* (in press).
- ⁵²M. J. Brennan, M. J. Day, S. J. Elliott, and R. J. Pinnington "Piezoelectric actuators and sensors," *Proceedings of the Active Control of Vibration IUTAM Symposium*, 5–8 September 1994, University of Bath, UK, 1994.
- ⁵³M. Gavagni, P. Gardonio, and S. J. Elliott, "Theoretical study of a velometer sensor-piezoelectric patch actuator pair for direct velocity feedback control systems," ISVR Technical Memorandum, 2004.
- ⁵⁴A. Poy, "Modelling matched piezoelectric sensor/actuator pairs for feedback control," M.Sc. thesis, University of Southampton, 2003.